Magnetic Reynolds number effects in compressible magnetohydrodynamic turbulence

F. Ladeinde
Mechanical Engineering, State University of New York at Stony Brook, Stony Brook, New York 11794-2300

D. V. Gaitonde
Air Vehicles Directorate, Air Force Research Laboratory, Wright-Patterson Air Force Base, Ohio 45433-7521

(Received 20 June 2003; accepted 10 March 2004; published online 4 May 2004)

The effects of the magnetic Reynolds number, Re_σ, on decaying two-dimensional compressible magnetohydrodynamic (MHD) turbulence are investigated through direct numerical simulations. The initial relative intensities of, and the correlation between, the fluctuating velocity (**u**) and magnetic induction (**b**) fields are also varied, as measured with the respective parameters f and angle θ. The investigations cover the parameter ranges $1 \leqslant \mathrm{Re}_\sigma \leqslant 250$, $0° \leqslant \theta \leqslant 90°$, and $1 \leqslant f \leqslant 3$. The results suggest that, at the lowest Re_σ investigated, the magnetic field has a negligible impact on the evolution of the turbulence kinetic energy E_k. At higher Re_σ values, when magnetic effects are important, the magnetic field tends to accelerate the decay of the turbulence energy relative to non-MHD flows. On the other hand, the magnetic energy E_b shows the opposite trend, being rapidly driven from its initial values to essentially zero very early in the transient at lower Re_σ values, while higher Re_σ values significantly retard this decay. An enhancement of density fluctuations is noted in the intermediate Re_σ range. An interesting observation pertaining to the normalized cross helicity is the fast decay to zero of this quantity when $\mathrm{Re}_\sigma = 1$, independent of the values of θ and f. That is, the fluctuating **u** and **b** fields tend to be uncorrelated when the magnetic Reynolds number is low. In this case, the role of the magnetic field is passive, and it is merely convected by the velocity field. The conditions required to maintain a high correlation during the evolution are discussed. We have also seen that the E_b decay mode is less sensitive to the value of θ than that of E_k. The relative contribution of E_k, E_b, and the internal energy E_i to the total energy E_t is discussed in relation to the values of f, θ, and Re_σ. © *2004 American Institute of Physics.* [DOI: 10.1063/1.1736674]

I. INTRODUCTION

The dynamics of electrically conducting fluid flows in the presence of magnetic forces have been studied extensively in fields as diverse as fusion physics,[1–4] astrophysics,[5–7] solar physics,[8–10] and material processing.[11] The present paper, however, is concerned with aerospace applications of the subject,[12,13] which is increasingly viewed as a pacing item for hypersonic flight. Although the knowledge that electrical and magnetic forces can have a profound influence on aerospace-related flows is not new,[14,15] the fundamental study of magnetohydrodynamics (MHD) turbulence in related canonical systems has not received enough attention. The parameters encountered in high-speed naturally or artificially ionized flows give rise to dynamics which are expected to be considerably different from those that have received attention in other fields. The behavior of the rugged invariants that come into play in turbulent MHD flows, notably the mean cross helicity, $H_c(\kappa) \equiv \frac{1}{2}\langle \mathbf{u}\cdot\mathbf{b} \rangle$, the mean magnetic helicity, $H_m(\kappa) \equiv \frac{1}{2}\langle \mathbf{a}\cdot\mathbf{b} \rangle$, and mean electric current helicity, $H_j(\kappa) \equiv \frac{1}{2}\langle \mathbf{j}\cdot\mathbf{b} \rangle$, has been investigated in such nonaerospace fields as astrophysics. Here, angular brackets denote spatial averaging, κ is the magnitude of the wave number vector, **u**, **b**, and **j** are the fluctuating components of the velocity, magnetic, and current fields, respectively, and **a** is the magnetic potential: $\mathbf{b} = \nabla \times \mathbf{a}$. Previous work has also reported on spectral anisotropy that is dynamically generated in MHD turbulence when a strong mean magnetic field $\mathbf{B}_0$ is present. For example, correlation lengths parallel to $\mathbf{B}_0$ were reported to be up to ten times the perpendicular scale in fusion-related machines.[16,17] Also, Moffat.[18] Sommeria and Morcau,[19] Davidson[20,21] reported on the suppression of homogeneous turbulence at moderate to large values of the interaction parameter, $N = \mathrm{Re}_\sigma R_b$, where Re_σ is the magnetic Reynolds number and R_b is the magnetic pressure number. Anisotropy, which is caused by the Lorentz force, has been reported for both decaying and forced MHD turbulence, and from theory, experiments, and numerical simulations. Zikanov and Thess[11] used direct numerical simulation (DNS) to study the transformation of initially isotropic turbulent flow of electrically conducting incompressible viscous fluid under the influence of an imposed homogeneous magnetic field. They considered magnetic Prandtl number $\mathrm{Pr}_m \ll 1$ and assumed small values for the magnetic Reynolds, Re_σ, a condition they used to justify the quasistatic approximation[22] and avoid the solution of the evolution equations for the magnetic induction field. Large scale forcing was applied on $\kappa \leqslant 2.5$, where κ is the wave number, in order to maintain a statistical steady state. The path of transformation, i.e., from isotropic to nonisotropic flow, depends on N. For small val-

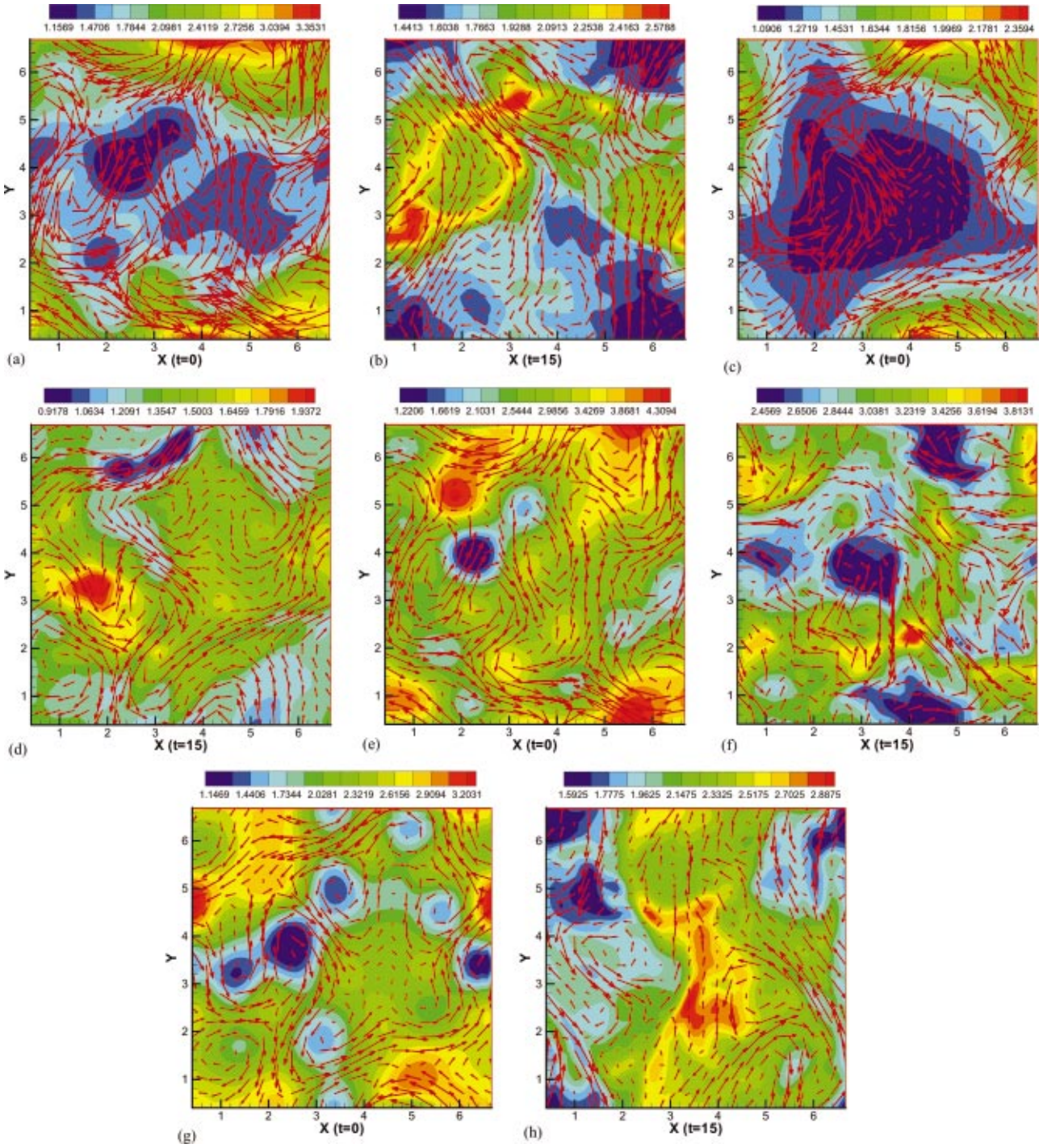

FIG. 1. (Color) Pressure and magnetic induction fields for selected cases in Table I: (a) f1-0-250 at $t=0$, (b) f1-0-250 at $t=15$, (c) f1-45-250 at $t=0$, (d) f1-45-250 at $t=15$, (e) f3-0-250 at $t=0$, (f) f3-0-250 at $t=15$, (g) f3-45-250 at $t=0$, (h) f3-45-250 at $t=15$. Note that the time t is in units of the eddy turnover time.

ues of N, the flow remains essentially isotropic. Intermediate N values lead to organized quasi-two-dimensional evolution lasting several eddy turnover times, which is interrupted by strong 3D turbulent bursts. For large values of N, there is strong anisotropy and significant suppression of turbulence, with the flow restricted to the perpendicular direction to $\mathbf{B}_0$. That is, only velocity modes with nonzero gradients in the direction of $\mathbf{B}_0$ is (Joule) dissipated; the velocity gradients in the direction of $\mathbf{B}_0$ are damped and vortical structures are elongated in this direction. The present effort builds on this analysis by considering compressibility and lifting the dual constraints of quasistatic simplification and the use of forcing to maintain statistical steady state.

The inverse cascade of magnetic helicity has also received some attention.[23] The significance of this phenomenon lies in the provision of a mechanism for generating large-scale fluctuating magnetic energy. The phenomenon has been reported for the case where $\mathbf{B}_0 \rightarrow 0$ at ∞ (nonhomo-

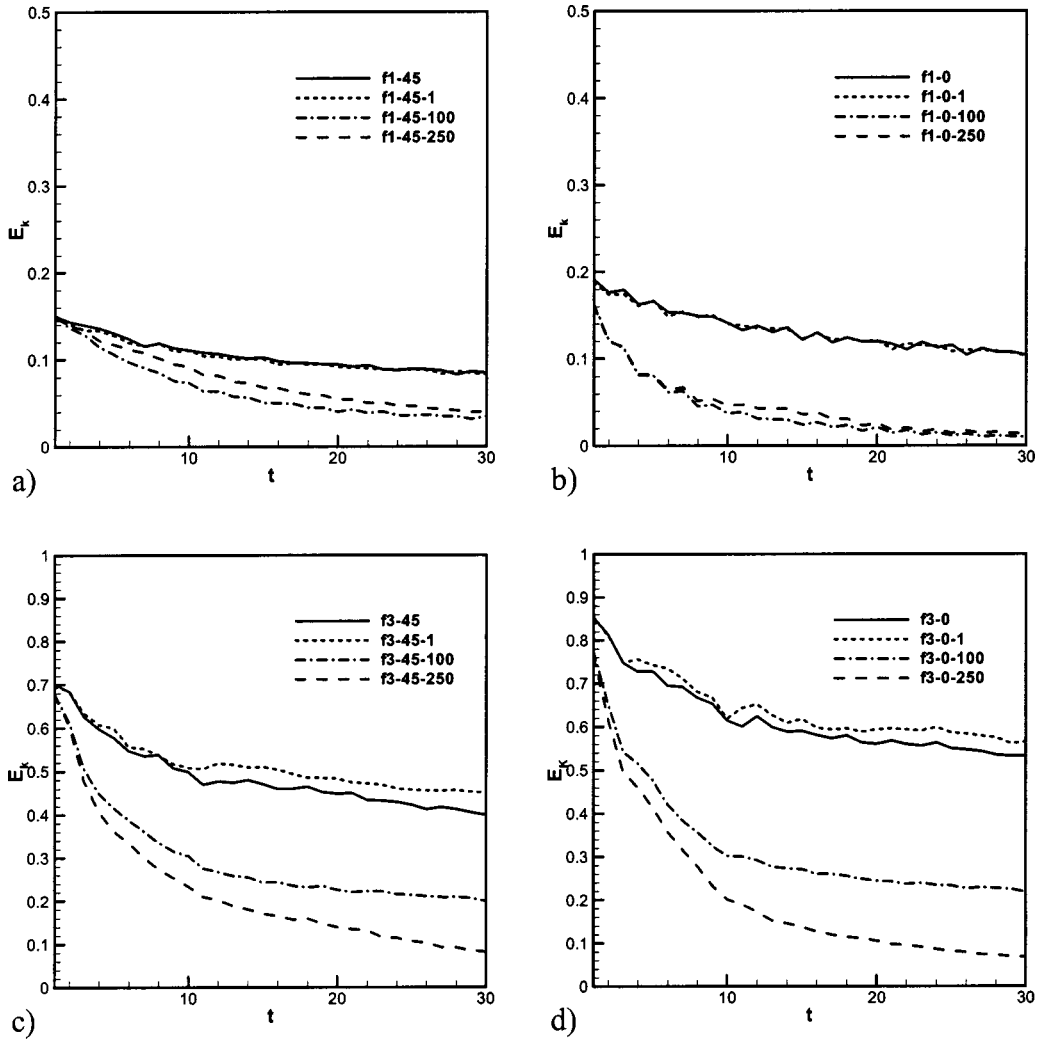

FIG. 2. Evolution of the kinetic energy E_k. Refer to the text and Table I for the various cases defined by the legend.

TABLE I. Case studies for the MHD turbulence DNS calculations.

Case No.	Case Reference	f_u, f_b	θ^o	Re_σ	Remarks
I	f1-45-250	2, 2	45	250	
II	f1-45-1	2, 2	45	1	
III	f1-45-100	2, 2	45	100	
IV	f1-0-1	2, 2	0	1	
V	f1-0-100	2, 2	0	100	
VI	f1-0-250	2, 2	0	250	
VII	f3-45-1	3, 1	45	1	
VIII	f3-45-100	3, 1	45	100	
IX	f3-45-250	3, 1	45	250	
X	f3-0-1	3, 1	0	1	
XI	f3-0-100	3, 1	0	100	
XII	f3-0-250	3, 1	0	250	
XIII[a]	f1-45	2, 2	45	N/A	No MHD
XIV[a]	f1-0	2, 2	0	N/A	No MHD
XV[a]	f3-45	3, 1	45	N/A	No MHD
XVI[a]	f3-0	3, 1	0	N/A	No MHD

[a]Cases XI–XIV do not involve MHD, although the initial conditions were calculated to match those for the corresponding MHD cases. Note that Re_σ is not used in the calculation of the initial conditions and that the parameters f_u, f_b, θ, and Re_σ have been introduced earlier in this paper.

geneous) or $\mathbf{B}_0 = 0$ (homogeneous). A proposed mechanism[24] starts out with the transfer of large scale momentum energy to the small scale momentum field. This is followed by a transfer of the energy to the small-scale magnetic field via the equipartition action of the Alfvén waves at the high wave numbers. The final step in the process is the back transfer of the small-scale magnetic energy to the large-scale magnetic energy field.

The three scaling laws of Kolmogorov for non-MHD turbulence have also been investigated for MHD turbulence. An energy spectrum with an exponent of $-2/3$ has been reported,[25] in contrast to the $-5/3$ law. This result is in agreement with those of Kraichnan[26] and Iroshnikov[27] MHD results for the second law of Kolmogorov (temporal decay of energy) have been obtained using the idea of the persistence of large scales together with results from Kraichnan and Ironshnikov. Compared to the non-MHD case, this leads to a different expression for the temporal decay. Gomez, Politano, and Pouquet[25] validated the foregoing results, as well as the MHD results for the structure functions (third

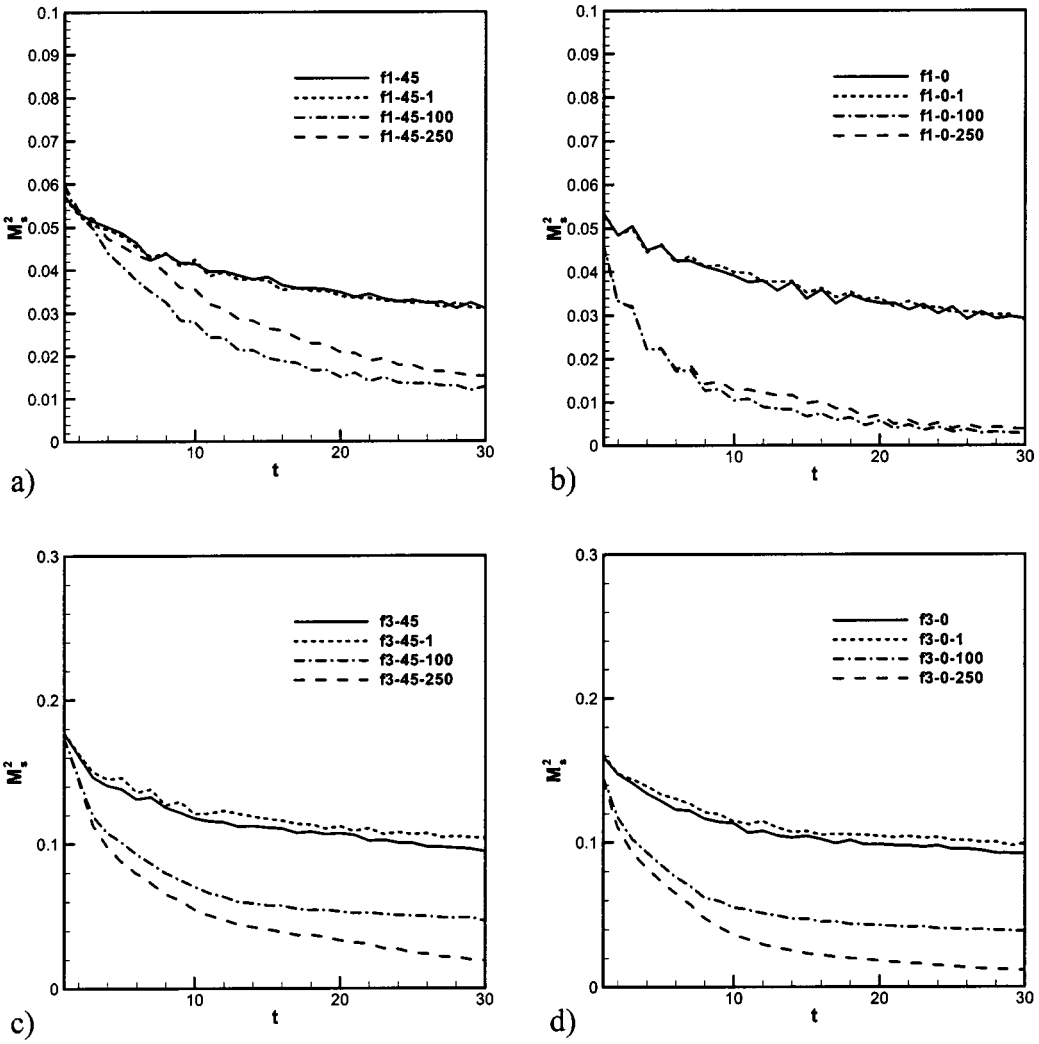

FIG. 3. Evolution of the square of the sonic Mach number, M_s^2. Refer to the text and Table I for the various cases defined by the legend.

law) in terms of the Elsässer variables $\mathbf{z}^{\pm} \equiv \mathbf{u} \pm \mathbf{b}$. However, more recent results by Muller and Biskamp[28] seem to suggest that MHD turbulence with finite magnetic helicity does not follow the phenomenology of Ironshnikov or Kraichnan, but agrees more with the Kolmogorov scaling. There is the implication that turbulence-Alfvén wave interaction does not control the turbulence dynamics, contrary to earlier suggestions.

Concerning intermittency, both temporal and spatial intermittency have been reported for turbulent MHD flows,[29]

TABLE II. Global statistics of the initial conditions. The initial conditions for cases XI–XIV match those for the corresponding MHD cases and are not repeated here.

Case No.	M_s	$\langle \mathbf{u}\cdot\mathbf{b} \rangle \equiv 2H_c$	$\langle \rho \mathbf{u}\cdot\mathbf{u} \rangle /2$	$\langle \mathbf{u}^2 \rangle$	$\langle \mathbf{b}\cdot\mathbf{b} \rangle /2$	E_i	R_{ub}
I	0.233	0.25	0.1551	0.25	0.125	0.030618	1.00
II	0.233	0.25	0.1551	0.25	0.125	0.030618	1.00
III	0.233	0.25	0.1551	0.25	0.125	0.030618	1.00
IV	0.224	2.979×10^{-4}	0.1762	0.25	0.125	0.078395	1.193×10^{-3}
V	0.224	2.979×10^{-4}	0.1762	0.25	0.125	0.078395	1.193×10^{-3}
VI	0.224	2.979×10^{-4}	0.1762	0.25	0.125	0.078395	1.193×10^{-3}
VII	0.433	0.333	0.7782	1.00	0.05556	0.06209	1.00
VIII	0.433	0.333	0.7782	1.00	0.05556	0.06209	1.00
IX	0.433	0.333	0.7782	1.00	0.05556	0.06209	1.00
X	0.408	3.973×10^{-4}	0.9283	1.00	0.05556	0.08563	9.27×10^{-4}
XI	0.408	3.973×10^{-4}	0.9283	1.00	0.05556	0.08563	9.27×10^{-4}
XI	0.408	3.973×10^{-4}	0.9283	1.00	0.05556	0.08563	9.27×10^{-4}

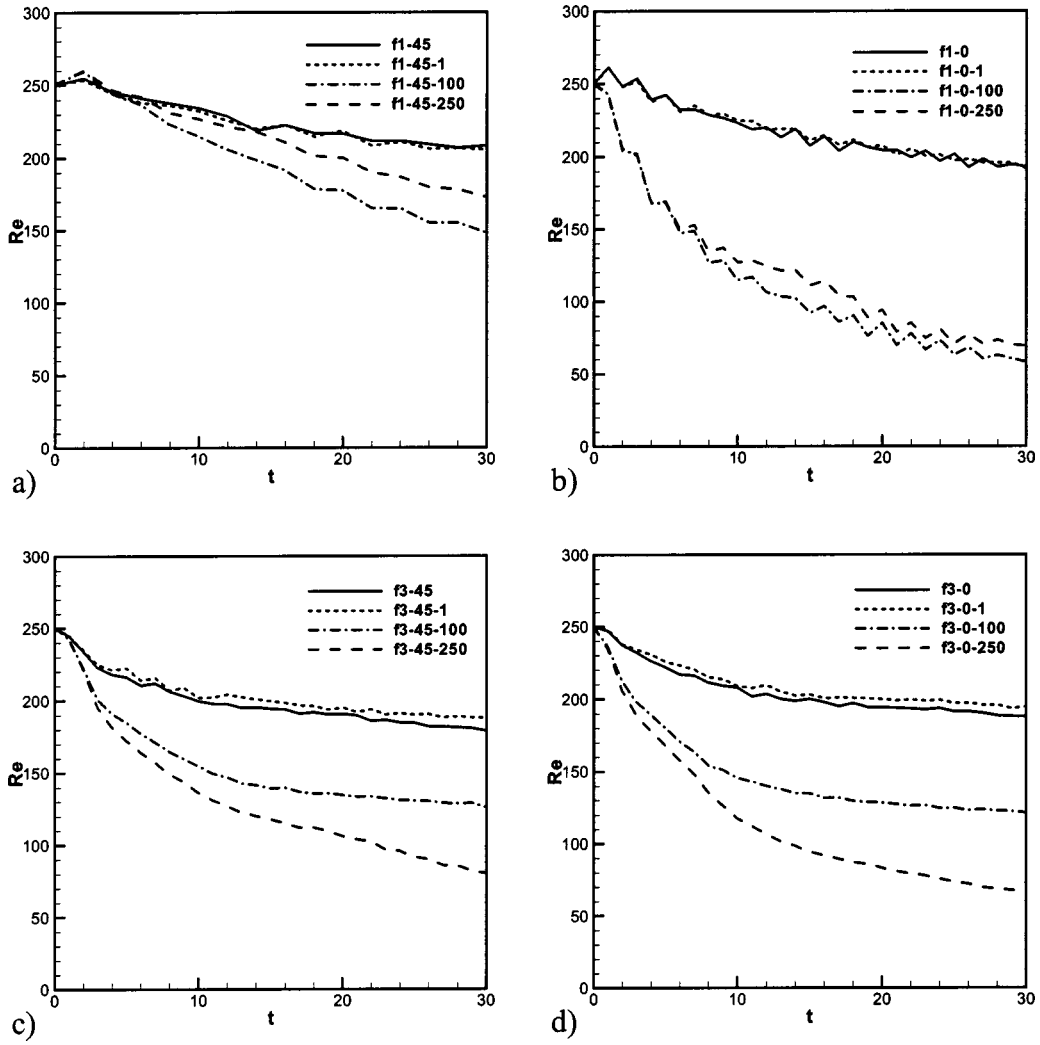

FIG. 4. Evolution of the turbulence Reynolds number normalized by the initial values of the root mean-squared velocity. Refer to the text and Table I for the various cases defined by the legend.

with 3D flows less intermittent than 2D, but more intermittent than 3D non-MHD turbulence. The physical variables $(\mathbf{u},\mathbf{b},\mathbf{z}^{\pm})$ tend to be more intermittent in the MHD case than in non-MHD and magnetic field could be as intermittent as the vorticity field.

The foregoing results pertain mostly to incompressible flows and therefore are not directly useful for aerospace applications, where the flow is compressible. Dahlburg and Picone,[30] Picone and Dahlburg,[31] and Ghosh and Matthaeus[32] have investigated compressible MHD flows, but they focused on nonaerospace applications. Dahlburg and Picone[30] examined the evolution of the Orszag–Tang vortex[29] in a 2D compressible medium. The initial conditions for the system consist of a nonrandom periodic field in which the magnetic and velocity fields contain X points but differ in modal structure along one spatial direction. Calculations were done for viscous and resistive Lundquist numbers of 50, 100, and 200, with Mach numbers in the range $0.1 \leqslant M_a \leqslant 0.6$. Compressible effects, which develop within one or two Alfvén transit times in this system, include the retardation of the growth of the correlation between **u** and **b**, the emergence of compressible small-scale structure as massive jets and the bifurcation of eddies in the compressible flow field. The studies were extended to the supersonic regime in a follow-up paper.[31]

Scaled and spectrally-filtered random initial conditions for the velocity and magnetic fields appear to be more suitable for aerospace applications[33] than the nonrandom Orszag–Tang vortex.[29] The systematic compressibility studies by Ghosh and Matthaeus[32] (hereafter referred to as GM1) used the former type of initial conditions and considered the characterization of three distinct time asymptotic types of behavior. Results for initial Mach numbers of 0.1 and 0.5 were compared to the incompressible results for a fixed value of the Alfvénic Mach number $M_2=1.0$ and magnetic Reynolds number $\mathrm{Re}_\sigma=250$. Three regions in the $E/A - E/2H_c$ diagram of Ting *et al.*[4] were examined. (E is the total energy, A is the mean squared magnetic potential, and H_c is cross helicity.) The study reported selective decay of kinetic energy when kinetic and magnetic energies were initially approximately equipartitioned. When the intensity of the magnetic fluctuations (b_{rms}) was significantly smaller than that of the velocity fluctuations (u_{rms}), a fast temporal dissipation of the magnetic energy was observed. The third

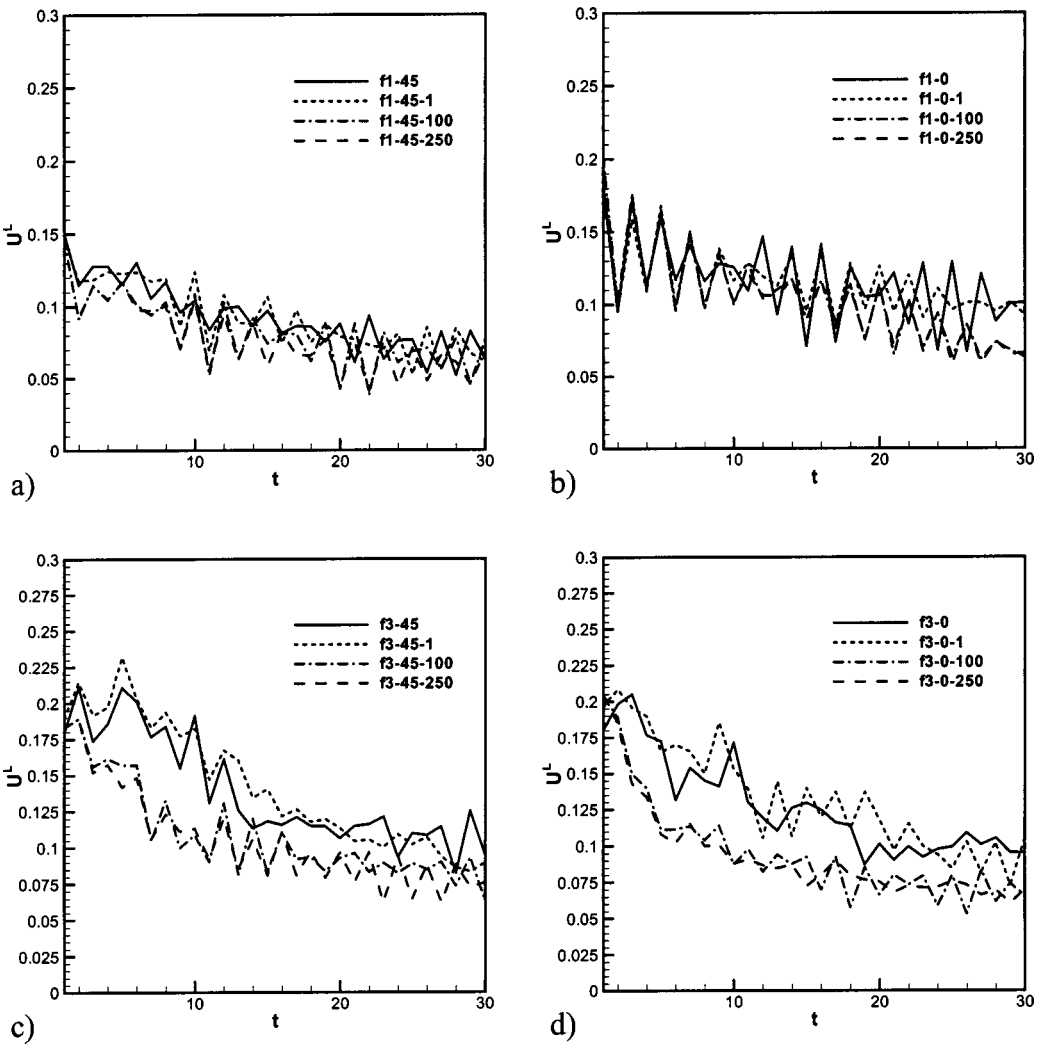

FIG. 5. Evolution of the longitudinal component of the velocity, U^L. Refer to the text and Table I for the various cases defined by the legend.

region examined in GM1 is characterized by highly correlated **u** and **b** fields in the initial flow. In time, the two fields tend to reach a constant energy ratio (Alfvén ratio) of order unity. The spectra of the kinetic, magnetic, and internal energies were reported for the three regions and were used to demonstrate the appearance of acoustic turbulence in the first and second regions discussed above.

The present paper differs from foregoing literature in several aspects. First, the emphasis on aerospace applications is new and implies small relative values of the electrical conductivity σ, as measured with the magnetic Reynolds number. For example, it is six to seven orders of magnitude smaller than in the astrophysical applications examined in GM1. It is also of interest to investigate the sensitivity of the results to a range of Re_σ values within $1.0 \leqslant \mathrm{Re}_\sigma \leqslant 250.0$. (Inclusion of Re_σ values in the high end of this range allows comparison with the results in GM1.)

An obvious limitation of the present work is the use of a 2D model, which requires that care be exercised in interpreting the results. This is a compromise, however. The number of parameters of dynamic significance is numerous, which, together with the inclusion of the MHD transport equations, prevents any extensive parametric 3D studies because of the current limitations in computer speed. Despite access to the most powerful supercomputers and a high-order accurate fully 3D simulation tool,[43] it was found unfeasible to explore the range of parameters of interest. Recent efforts using multiprocessing strategies[44] show promise of lifting these constraints and we expect to obtain selective 3D results in the future. Note that studies based on the quasistatic approximations, such as in Kassinos, Knaepen, and Carati,[34] can afford to calculate full 3D models because the MHD transport equations are not solved. Note that the simulations in GM1 as well as those in the papers by Dhalburg and Picone, included the MHD equations and were also based on a 2D model. Nevertheless, they reported reasonable results that agree well with the expected physics, with the suggestion that a carefully studied 2D model could provide useful information on the real system. In order to reduce spectral energy back transfer resulting from the use of 2D calculations, we remove the first spectral mode when calculating some of the turbulence quantities.

The governing equations are presented in Sec. II, followed by a detailed description of the initial condition specification and generation in Sec. III. Section IV summarizes the numerical procedure for calculating the various equa-

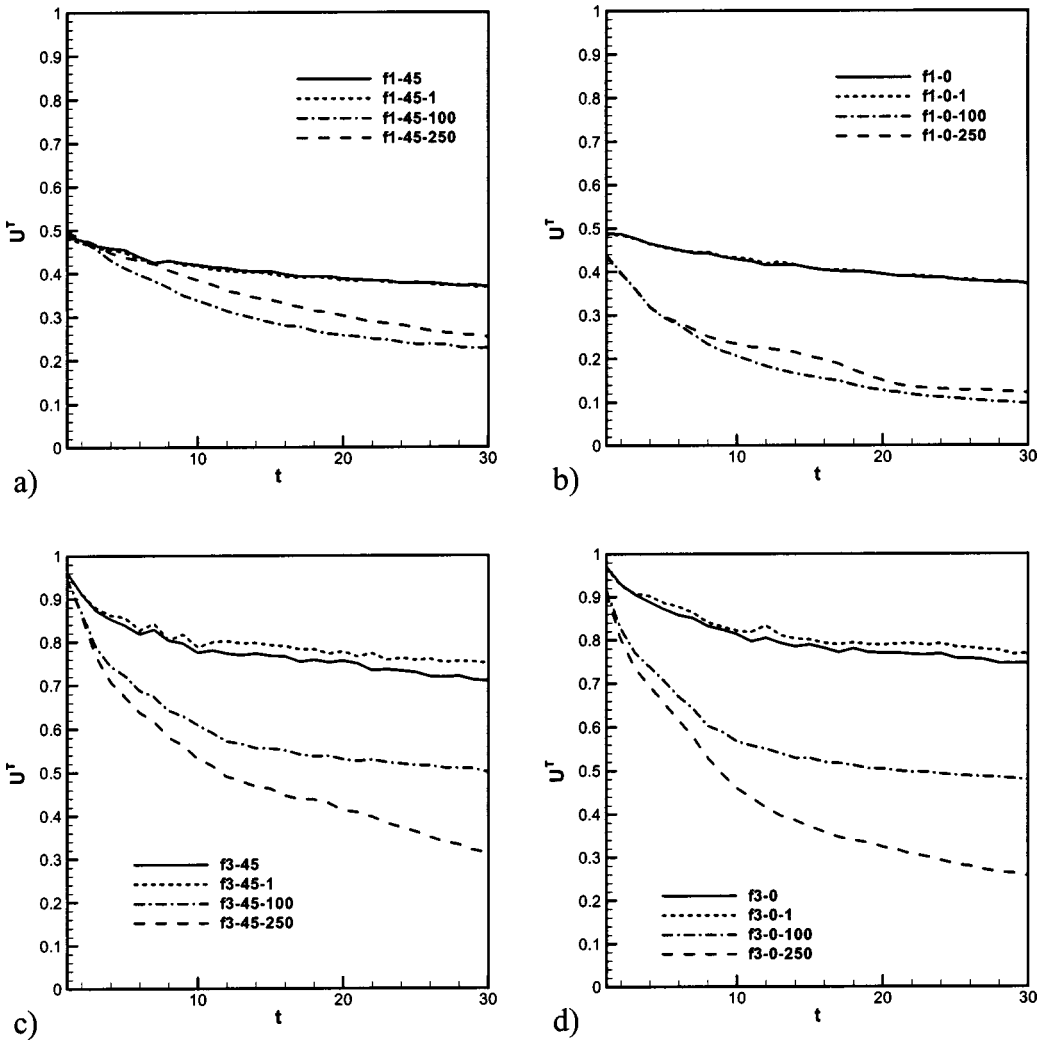

FIG. 6. Evolution of the transverse component of the velocity, U^T. Refer to the text and Table I for the various cases defined by the legend.

tions, while Sec. V discusses the various case studies. Results are presented in Sec. VI, followed by concluding remarks in Sec. VII.

II. GOVERNING EQUATIONS

The MHD equations are solved in dimensionless form, with the scales L_0, U_0, L_0/U_0, ρ_0, P_0, T_0, B_0, k_0, μ_0, μ_{m_0}, and σ_0 for length, velocity, time, density, pressure, temperature, magnetic induction field, thermal conductivity, dynamic viscosity, magnetic permeability, and electric conductivity, respectively. The equations take the following form:

$$\frac{\partial \rho}{\partial t} + \nabla \cdot (\rho \mathbf{u}) = 0, \tag{1}$$

$$\frac{\partial}{\partial t}(\rho \mathbf{u}) + \nabla \cdot \left(\rho \mathbf{u}\mathbf{u} - \frac{R_b}{\mu_m}\mathbf{B}\mathbf{B} + P\mathbf{I} \right) - \frac{1}{\mathrm{Re}} \nabla \cdot \boldsymbol{\tau} = \mathbf{0}, \tag{2}$$

$$\frac{\partial \mathbf{B}}{\partial t} + \nabla \cdot (\mathbf{u}\mathbf{B} - \mathbf{B}\mathbf{u}) + \frac{1}{\mathrm{Re}_\sigma} \nabla \times \left[\frac{1}{\sigma} \left(\nabla \times \frac{\mathbf{B}}{\mu_m} \right) \right] = \mathbf{0}, \tag{3}$$

$$\frac{\partial \rho E}{\partial t} + \nabla \cdot (\rho E + P)\mathbf{u} - R_b \nabla \cdot \mathbf{B} \left(\mathbf{u} \cdot \frac{1}{\boldsymbol{\mu}_\mathbf{m}} \mathbf{B} \right) - \frac{1}{\mathrm{Re}} \nabla \cdot (\mathbf{u} \cdot \boldsymbol{\tau}) - \frac{1}{(\gamma - 1)\mathrm{Pr}\, M_1^2\, \mathrm{Re}} \nabla \cdot k \nabla \mathbf{T} + \frac{R_b}{\mathrm{Re}_\sigma} \nabla \cdot \left[\frac{1}{\mu_m \sigma} \mathbf{B} \cdot \nabla \frac{1}{\mu_m} \mathbf{B} - \nabla \frac{1}{\mu_m} \mathbf{B} \cdot \frac{1}{\mu_m \sigma} \mathbf{B} \right] = 0. \tag{4}$$

The governing equations for the magnetic field induction have been obtained by combining the Ampère–Maxwell Law, Faraday's Law, and Ohm's Law. Although the total energy equation is solved in the form of Eq. (4) above in our code, the nondimensional equation of state used in the present paper is $p = \rho^\gamma$, meaning that Eq. (4) is internally transformed in our code to be consistent with the equation of state. γ, the ratio of specific heats, is kept constant at 5/3 for all the results in this paper. The length scale is the integral scale of the initial field, or $\pi/2u_{\mathrm{rms}}^2 \int_0^\infty \kappa^{-1} E(\kappa) d\kappa$, where u_{rms} and $E(\kappa)$ are the respective values of the root mean-squared velocity fluctuation and energy spectrum of the ini-

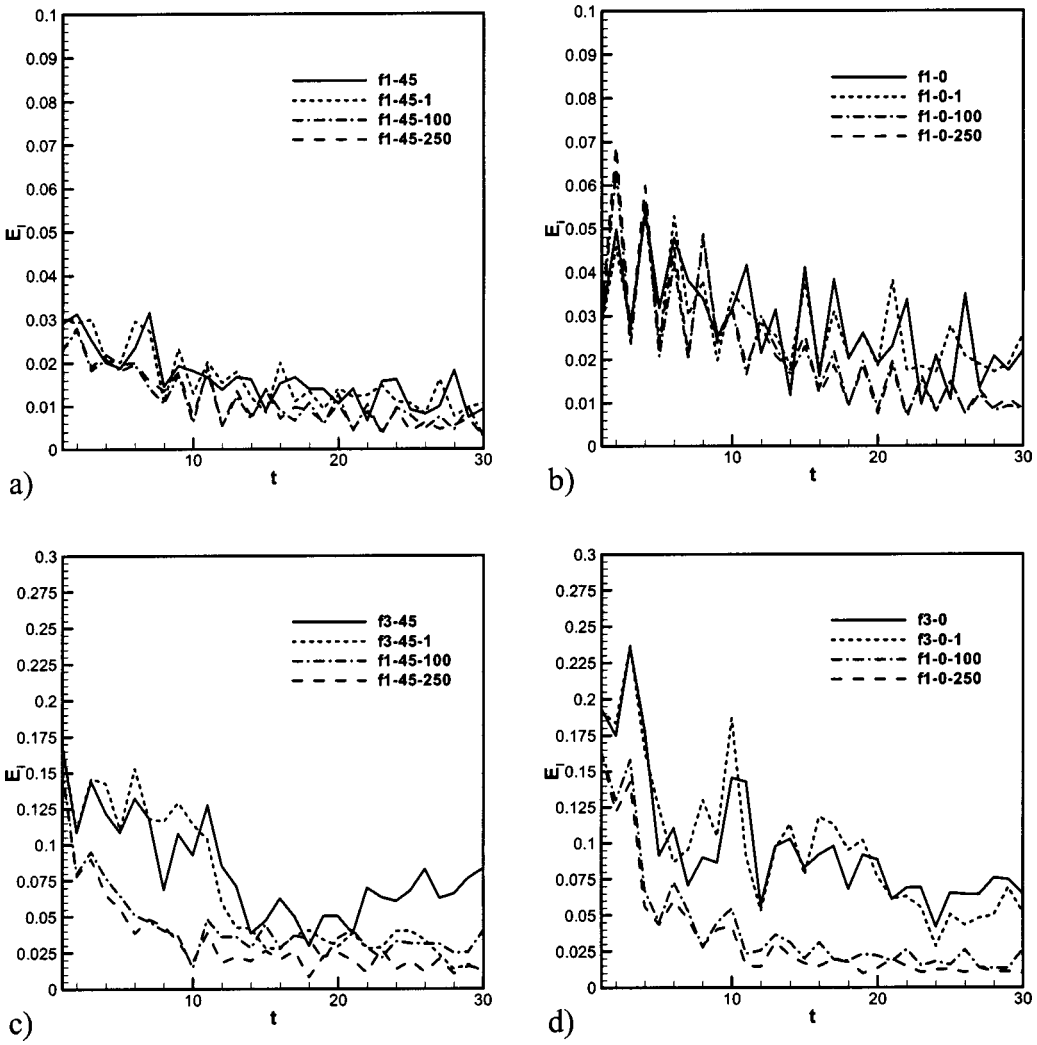

FIG. 7. Evolution of the internal energy E_i. Refer to the text and Table I for the various cases defined by the legend.

tial field. Note that the length scale has a nondimensional value of unity at all times, even though the integral length is time-dependent.

The independent variables of the problem are time, t, and the spatial coordinate directions $\mathbf{x}\equiv(x,y,z)$. The primary dependent variables are density ρ, the velocity components $\mathbf{u}\equiv(u,v,w)$, the components of the magnetic induction field, $\mathbf{B}\equiv(B_x,B_y,B_z)$, and the total energy, ρE. The temperature, T, also appears, as does the reduced pressure $P=p+R_b(|\mathbf{B}|^2/2\mu_m)$ and total energy $\rho E=[p/(\gamma-1)]+\frac{1}{2}\rho|\mathbf{u}|^2+R_b(|B|^2/2\mu_m)$. The parameters of the problem include the nondimensional thermal conductivity, k, dynamic viscosity, μ, magnetic permeability, μ_m, electric conductivity, σ, the Prandtl number, $\mathrm{Pr}=C_p\mu_0/k_0$, where C_p is the specific heat at constant pressure, the characteristic sonic Mach number, $M_1=U_0/C_s$, where C_s is a characteristic sound speed, the magnetic pressure number, $R_b=B_0^2/\rho_0U_0^2\mu_{m_0}$, the hydrodynamic Reynolds number, $\mathrm{Re}=\rho_0U_0L_0/\mu_0$, and the magnetic Reynolds number, $\mathrm{Re}_\sigma=U_0L_0/(\mu_{m_0}\sigma_0)^{-1}\equiv U_0L_0/\eta_0$. The viscous stress tensor $\boldsymbol{\tau}$ has its usual definition:

$$\boldsymbol{\tau}=\mu(\nabla\mathbf{u}+\nabla\mathbf{u}^*)-\tfrac{2}{3}\mu\nabla\cdot\mathbf{u},$$

where an asterisk on a quantity denotes a transpose operation on the quantity. Other parameters can be defined, such as the characteristic Alfvénic Mach number M_2 (Ghosh and Matthaeus[32]), which can written as $M_2=(R_b/\mu_m)^{-1/2}$. Also, the use of the Alfvén's velocity $U_A=B_0/(\rho_0\mu_{m_0})^{1/2}$ in the definitions of the hydrodynamic (Re) and magnetic (Re_σ) Reynolds numbers, respectively, gives the viscous and resistive Lundquist numbers S_v and S_r used by Dahlburg and Picone.[30] This equivalence occurs when $M_2=1$. It is easily shown that the instantaneous value of the interaction parameter, N, is $N_0\sigma/(u_{\mathrm{rms}}\rho)$, where N_0 is the product of the magnetic Reynolds number and the magnetic pressure number in the initial field. Thus, with $R_b=1$ in the initial field, $1\leqslant N_0\leqslant 250$. The nondimensional eddy turnover time, T_E, is equal to $1/\langle u_{\mathrm{rms}}\rangle$, where u_{rms} is the nondimensional root-mean squared turbulence velocity. The nondimensional calculation time, that is, the time that appears in the governing Eqs. (1)–(4), is denoted by t. The number of eddy turnover time units is therefore equal to $t\langle u_{\mathrm{rms}}\rangle$, where

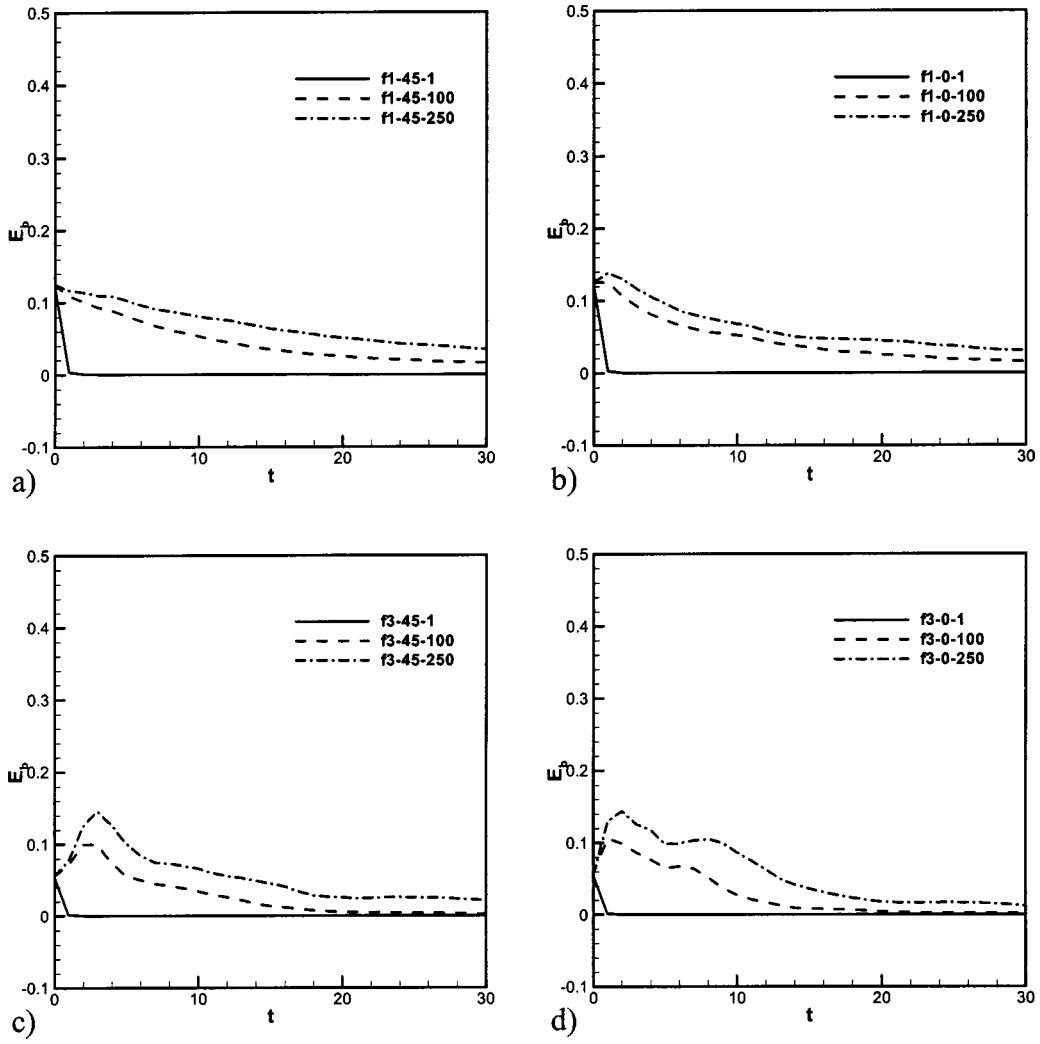

FIG. 8. Evolution of $E_b \equiv R_b \langle \mathbf{b}\cdot\mathbf{b} \rangle / 2\mu_m$.

$$\langle u_{\mathrm{rms}} \rangle (t) = \frac{1}{t} \int_0^t u_{\mathrm{rms}}(t)\, dt.$$

Note that this integral gives the (nondimensional) distance travelled by an eddy over a (nondimensional) time period t. Standard averaging over the grid points is used to compute u_{rms} at each time step and u_{rms} is used to represent the velocity of an eddy at each instant of time. Hence, $\langle u_{\mathrm{rms}} \rangle (t)$ represents a pseudoconvective velocity at time t. Information on the variation of u_{rms} with time can be gleaned from the Re plot since $\mathrm{Re}(t) = \mathrm{Re}_0 * u_{\mathrm{rms}(t)} / u_{\mathrm{rms}(t=0)}$, where Re_0 denotes the value of the specific (initial) hydrodynamic Reynolds number.

III. INITIAL CONDITIONS

The calculation of the initial fields **u** and **b** starts with the generation of random numbers in $(-1,1)$ for the fields. The corresponding spectral fields $\hat{\mathbf{u}}$ and $\hat{\mathbf{b}}$ are generated and the incompressible components $\hat{\mathbf{u}}^I = \hat{\mathbf{u}} - (\mathbf{k}\cdot\hat{\mathbf{u}}/k^2)\mathbf{k}$, $\hat{\mathbf{b}}^I = \hat{\mathbf{b}} - (\mathbf{k}\cdot\hat{\mathbf{b}}/k^2)\mathbf{k}$ are determined, where **k** is the wave number vector, with magnitude k. These fields are then filtered with the energy $E=1$ for $1 \leqslant k \leqslant \sqrt{12}$ and then scaled with the energy in each mode. This "tophat" spectra initial energy distribution has been widely used in compressible turbulence literature,[32,35,45] as well as in DNS of chemically reacting flows. The spectrum, which is basically a filter for the "energy" from the random fields, allows only a few modes in the initial field (approximately 10 in 2D or 3 in each of the two coordinate directions). A detailed description of the generation of this aspect of the initial conditions is available.[35]

The correlation between the otherwise random velocity and magnetic induction fields has been obtained using two different methods. The first consists of generating the random fields in Fourier space and introducing a phase angle between the two fields (GM1). Random numbers for vorticity $\omega(\mathbf{k})$ and the magnetic potential $a(\mathbf{k})$ are generated:

$$\omega(\mathbf{k}) = C_1 \sum_{1 \leqslant |\mathbf{k}|^2 \leqslant 12} |\mathbf{k}| e^{i[2\pi R(\mathbf{k}) \pm \theta}},$$

$$a(\mathbf{k}) = C_2 \sum_{1 \leqslant |\mathbf{k}|^2 \leqslant 12} \frac{1}{|\mathbf{k}|} e^{i[2\pi R(\mathbf{k})]},$$

where $R(\mathbf{k})$ is a unique random number for each wave number vector **k**, and θ is the phase angle between the initial

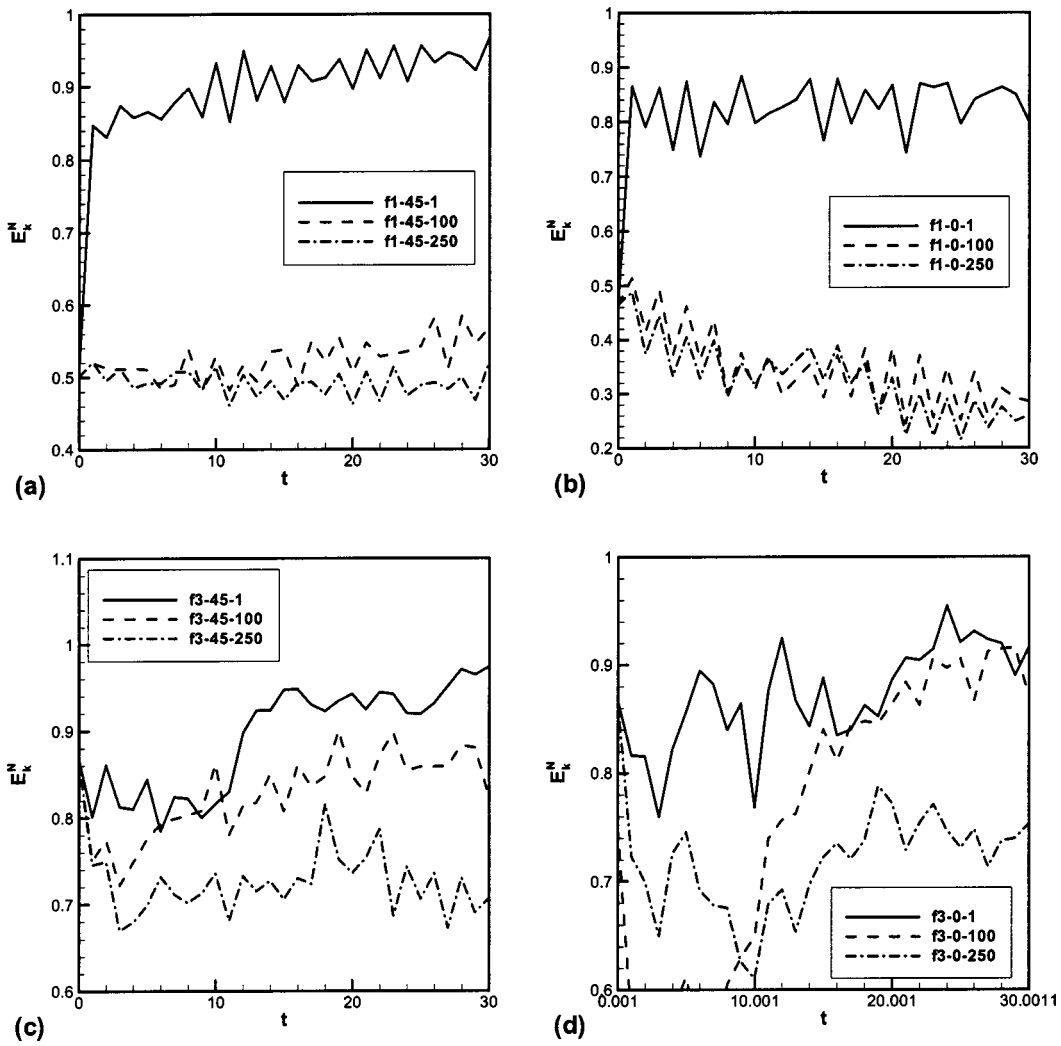

FIG. 9. Fractional contribution of the turbulence kinetic energy to the total energy. Refer to the text and Table I for the various cases defined by the legend.

vector potential and vorticity. The corresponding velocity and magnetic induction fields are obtained as

$$\mathbf{u}(\mathbf{k}) = \mathbf{k} \times \hat{\mathbf{z}}\omega(\mathbf{k})/|\mathbf{k}|^2,$$

$$\mathbf{b}(\mathbf{k}) = \mathbf{k} \times \hat{\mathbf{z}}a(\mathbf{k})/|\mathbf{k}|^2.$$

An alternative approach involves taking the physical space random results $\mathbf{u}'$ and $\mathbf{b}'$ and correlating them:

$$\begin{bmatrix} \mathbf{u} \\ \mathbf{b} \end{bmatrix} = \begin{bmatrix} \cos\theta & \sin\theta \\ \sin\theta & \cos\theta \end{bmatrix} \begin{bmatrix} \mathbf{u}' \\ \mathbf{b}' \end{bmatrix}. \tag{5}$$

The results reported in this paper were obtained with this approach. The correlated fields are subsequently scaled: $\mathbf{u} \leftarrow \mathbf{u}/(f_u u_{\mathrm{rms}})$ and $\mathbf{b} \leftarrow \mathbf{b}/(f_b b_{\mathrm{rms}})$, where $u_{\mathrm{rms}} = [\langle |\mathbf{u}(\mathbf{x})|^2 \rangle]^{1/2}$ and $b_{\mathrm{rms}} = [\langle |\mathbf{b}(\mathbf{x})|^2 \rangle]^{1/2}$. For the procedure outlined above, we have found that the quantities $f \equiv f_b f_u$ and θ are very important to the statistics of the initial field, such as the Alfvén ratio $r_A = \langle \mathbf{u} \cdot \mathbf{u} \rangle / \langle \mathbf{b} \cdot \mathbf{b} \rangle$, cross helicity $H_c = \langle \mathbf{u} \cdot \mathbf{b} \rangle / \mathbf{2}$, the rms values of the flow and magnetic induction fields, and the initial eddy turnover time scale, T_E. Specifically, the simple relation, $\langle \mathbf{u} \cdot \mathbf{b} \rangle = 1/f$ results for $\theta = 45°$, while $\langle \mathbf{u} \cdot \mathbf{b} \rangle_{30°} = \langle \mathbf{u} \cdot \mathbf{b} \rangle_{60°} = \sqrt{3}/2f$ and $r_A = (f_b/f_u)^2$. (Here, $\langle \mathbf{u} \cdot \mathbf{b} \rangle_\phi$ denotes the value of $\langle \mathbf{u} \cdot \mathbf{b} \rangle$ when $\theta = \phi°$.) We are not aware of these correlations in the literature. Note that the conditions $\langle \mathbf{u} \cdot \mathbf{u} \rangle = \langle \mathbf{b} \cdot \mathbf{b} \rangle = \mathbf{1}$ can be obtained with $f_u^2 = f_b^2 = r_A = 1$. The cases $\theta = 0°$ and $\theta = 45°$ are studied in this paper. It is pointed out that $\theta = 0°$ results in an identity transformation in Eq. (5), meaning that the original randomly generated **u** and **b** fields are used in this particular case.

The velocity and magnetic induction fields obtained from the foregoing procedure are used in the calculation of the initial fluctuating pressure field $p(\mathbf{x})$ via the incompressible flow relation

$$\nabla \cdot (\nabla \cdot \rho \mathbf{uu}) + \nabla^2 p - \frac{R_b}{\mu_m} \nabla \cdot (\mathbf{bb}) + \frac{R_b}{2\mu_m} \nabla^2 \mathbf{b}^2 = 0. \tag{6}$$

The pseudosound density correction is obtained using the procedure for the non-MHD SVPS case in Ladeinde *et al.*[35]

For decaying turbulence simulation such as the present one, the state of the initial flow determines the evolution pattern for prescribed parameter values. In the present study, a wide range of statistics has been investigated. The total energy E_t is defined as $E_t = E_k + E_b + E_i$, where $E_b = (R_b/\mu_m)\langle \mathbf{b} \cdot \mathbf{b} \rangle/2$ is the magnetic energy and E_i is the internal energy associated with the polytropic equation of state:

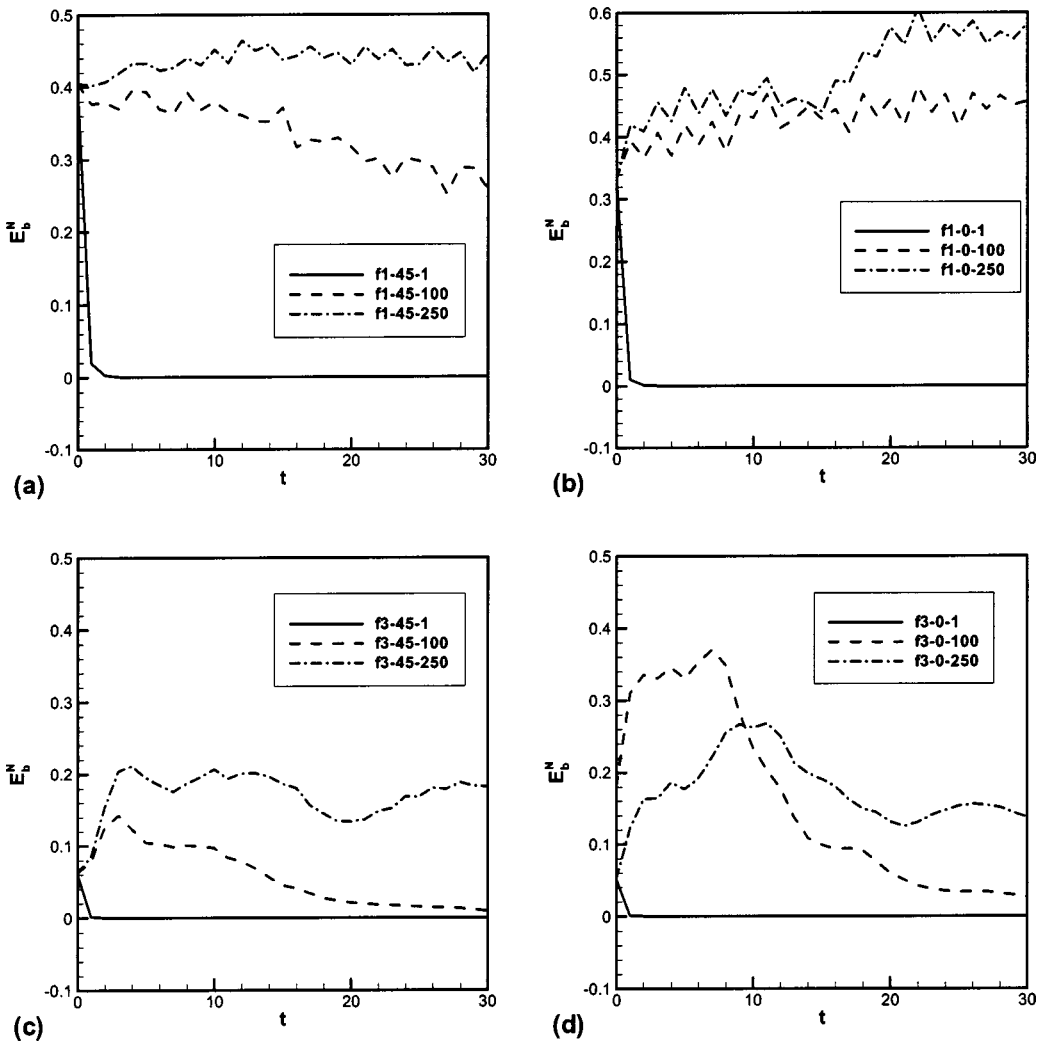

FIG. 10. Fractional contribution of the fluctuating magnetic energy to the total energy. Refer to the text and Table I for the various cases defined by the legend.

$$E_i \equiv \frac{(\langle \rho^\gamma \rangle - \langle \rho \rangle^\gamma)}{M_1^2 \gamma(\gamma-1)}, \tag{7}$$

where γ, the ratio of specific heats, is specified as 5/3 everywhere in the calculation domain. The instantaneous sonic number of the turbulent flow is defined as $M_s(t) = u_{\mathrm{rms}}(t)/\langle c_s(\mathbf{x},t)\rangle$, with $c_s(\mathbf{x}) = \rho(\mathbf{x})^{(\gamma-1)/2}/M_1$. Note that in simulations where $\langle \mathbf{u}\cdot\mathbf{u}\rangle = 1$ for the initial field and $M_s = \langle M_s^2(\mathbf{x})\rangle^{1/2}$, $M_1 \neq M_s$ because the pseudosound density correction is nonzero. Therefore, the deviation of M_s from M_1 is a statement of the integral deviation of the local density from $\rho = 1$, or the pseudosound density correction from zero. On the other hand, the condition $M_2 = M_a$ will be satisfied for the simulations in which $\langle \mathbf{b}\cdot\mathbf{b}\rangle = 1$ in the initial field, where $M_a = \langle M_a^2(\mathbf{x})\rangle^{1/2}$ and $M_a(\mathbf{x}) = M_2 \rho^{1/2}(\mathbf{x})|\mathbf{u}(\mathbf{x})|/|\mathbf{b}(\mathbf{x})|$.

The spectral internal energy distributions have been obtained in this work as a way of assessing the level of acoustic turbulence. This quantity is obtained as

$$P_i(i) = \frac{1}{n} \sum_{i-1/2 \leqslant k \leqslant i+1/2} \left| \mathrm{FFT}\left(\sqrt{\frac{\rho^\gamma}{M_1^2 \gamma(\gamma-1)}} \right) \right|^2,$$

where n refers to the number of modes in an annulus for the bin in spectral space. The kinetic and magnetic energy spectra $P_k(i)$ and $P_m(i)$ were also calculated:

$$P_k(i) = \frac{1}{n} \sum_{i-1/2 \leqslant k \leqslant i+1/2} |\mathrm{FFT}(\sqrt{\rho}\mathbf{u})|^2,$$

$$P_m(i) = \frac{1}{n} \sum_{i-1/2 \leqslant k \leqslant i+1/2} |\mathrm{FFT}(\mathbf{b})|^2.$$

Other quantities that have been studied in this paper as a function of Re_σ include the longitudinal U^L and transverse U^T velocity components.

An attempt was made to locate the parameter space for our calculations inside Fig. 1 of GM1, which was originally

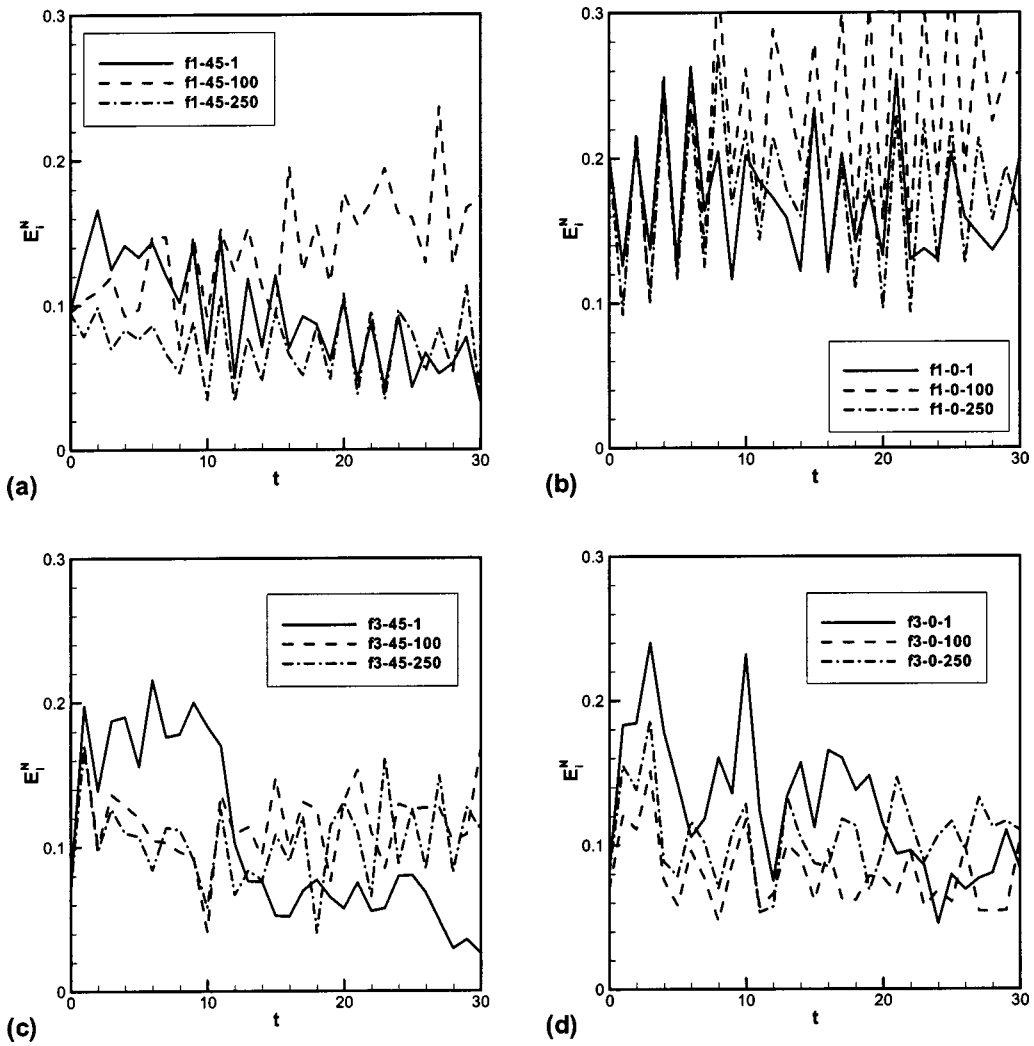

FIG. 11. Fractional contribution of the internal energy to the total energy. Refer to the text and Table I for the various cases defined by the legend.

developed for incompressible MHD flows. Because **b** and **u** in the initial fields are incompressible in the present work, it is the initial fields for ρ and p that determine whether we stay within the diagram. We have found that many ρ fields satisfying the pseudosound initial conditions used in this paper give values of E/A and $E/2H_c$ for the resulting compressible field (i.e., in terms of the compressible analogs of these two variables) that are located outside of the diagram. No attempt was made in this paper to force the compressible data to fit into the chart. The initial fields for pressure and the magnetic induction are shown in Fig. 1, along with the distribution of the fields when $t=15$. Tables I and II show some global statistics of the initial fields.

Finally, removing the nonsolenoidal component of **b** produces a field with $\nabla\cdot\mathbf{b}\sim 10^{-6}$ compared to unity, whereas $\nabla\cdot\mathbf{b}\sim O(1)$, otherwise.

IV. NUMERICAL SOLUTION

The majority of fundamental simulation of MHD turbulence[29,30,32] have been based on the spectral method. The present investigation, however, is based on the finite-difference method, which is less efficient for the problem at hand. This choice has been motivated by the need to extend our analysis to engineering problems with more complex geometrics and boundary conditions and for which the spectral method does not perform efficiently. The implementation of the high-order Padé schemes in Gaitonde and Visbal[36] is used, whereby Eqs. (1)–(4) are written in the following strong conservation form in generalized curvilinear coordinates (ξ,η,ζ):

$$\frac{\partial X'}{\partial \tau}+\frac{\partial F'}{\partial \xi}+\frac{\partial G'}{\partial \eta}+\frac{\partial H'}{\partial \zeta}=\frac{\partial F'_v}{\partial \xi}+\frac{\partial G'_v}{\partial \eta}+\frac{\partial H'_v}{\partial \zeta}+S', \tag{8}$$

where τ is the time domain, (ξ,η,ζ) are the transformed coordinates that respectively correspond to the physical coordinates (x,y,z). F', G', and H' are vectors of the inviscid fluxes while F'_v, G'_v, and H'_v are the fluxes associated with the stresses, and S' represents the source terms in the equations. Our code also allows the use of the weighted essentially nonoscillatory (WENO) finite difference schemes[37] when the Mach number is high enough to introduce shock waves into the calculations. Although the results in the

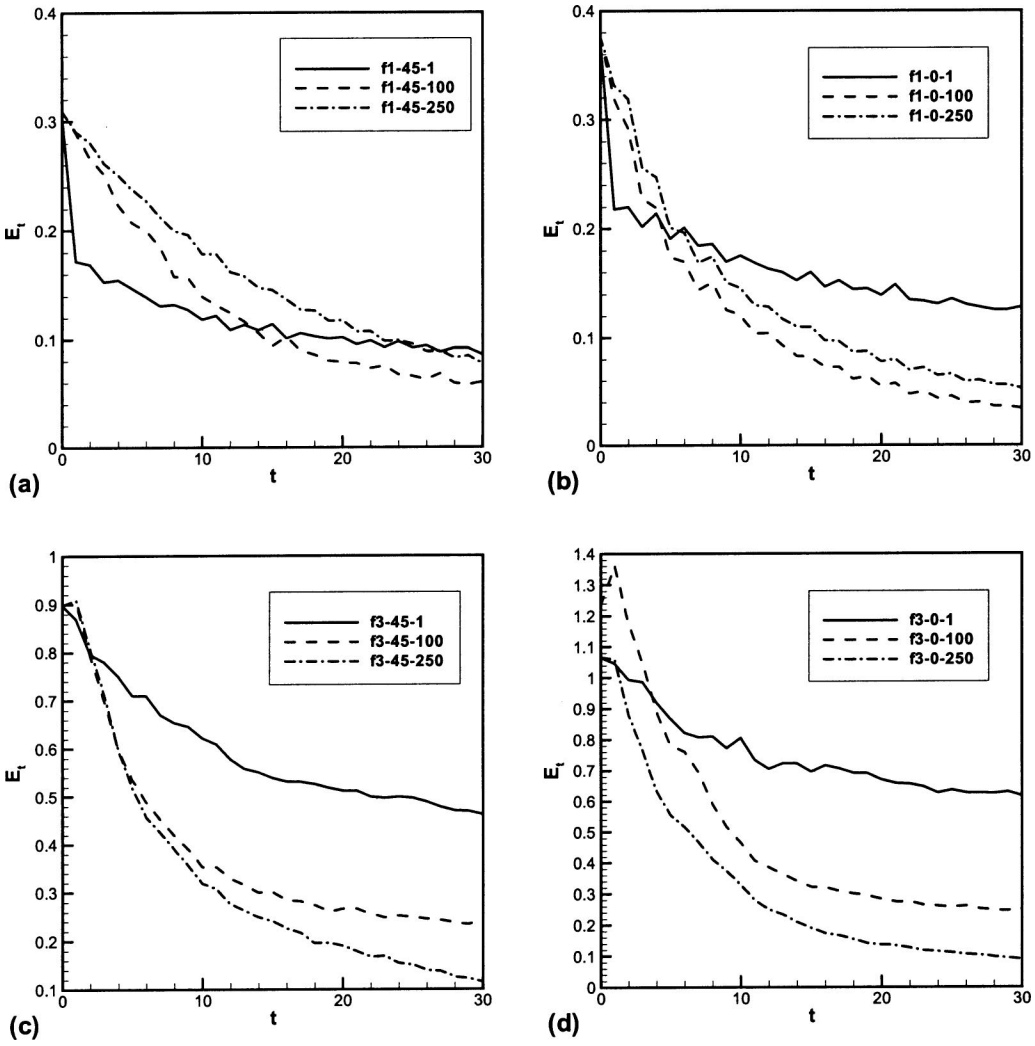

FIG. 12. Evolution of the total energy. Refer to the text and Table I for the various cases defined by the legend.

present paper are for regular geometries and moderate Mach numbers, the same formulations have been used for DNS in non-Cartesian geometries[38] and flow fields with shock waves.[39–41]

TABLE III. Partition of the total energy into its components at the end of simulation. Note that E_i is oscillatory, so that the data in this table cannot be used to predict a trend involving E_i. The figures for the evolution of this quantity should be used in conjunction with this table.

Case reference	E_k(%)	E_b(%)	E_i(%)	E_t
f1-45-1	96.59	0.862	3.323	0.0859
f1-45-100	56.65	25.854	17.50	0.0606
f1-45-250	51.814	44.44	3.75	0.0777
f1-0-1	79.88	0.601	20.00	0.12835
f1-0-100	28.54	45.69	25.77	0.03398
f1-0-250	25.90	58.15	15.94	0.05259
f3-45-1	97.39	.0755	2.60	0.4617
f3-45-100	82.475	0.9	16.62	0.2406
f3-45-250	70.63	18.18	11.18	0.1149
f3-0-1	91.61	0.0647	8.39	0.6168
f3-0-100	87.03	2.675	10.29	0.2505
f3-0-250	75.30	13.703	10.99	0.0896

With the compact schemes, the derivative u' for a generic variable u is obtained from the representation

$$\alpha u'_{i-1} + u'_i + \alpha u'_{i+1} = b\,\frac{u_{i+2}-u_{i-2}}{4\Delta\xi} + a\,\frac{u_{i+1}-u_{i-1}}{2\Delta\xi}, \tag{9}$$

where α, a, and b are constants that determine the spatial properties of the algorithm. The base compact differencing schemes used in this paper are the three-point, fourth-order scheme, C4, with $(\alpha,a,b)=(\frac{1}{4},\frac{3}{2},0)$, and the five-point, sixth-order scheme, C6, with $(\alpha,a,b)=(\frac{1}{3},\frac{14}{9},\frac{1}{9})$. Note that the symbol u above also represents components of vector quantities, such as the F' vector.

The formula in Eq. (9) is used to calculate the various derivatives in the (ξ,η,ζ) plane, as well as the metrics of the coordinate transformation. The derivatives of the inviscid fluxes are obtained by first forming these fluxes at the nodes and subsequently differentiating each component with the above formulas. In order to reduce error on stretched meshes, the required metrics are computed with the same scheme that is employed for the fluxes. To form the second derivative

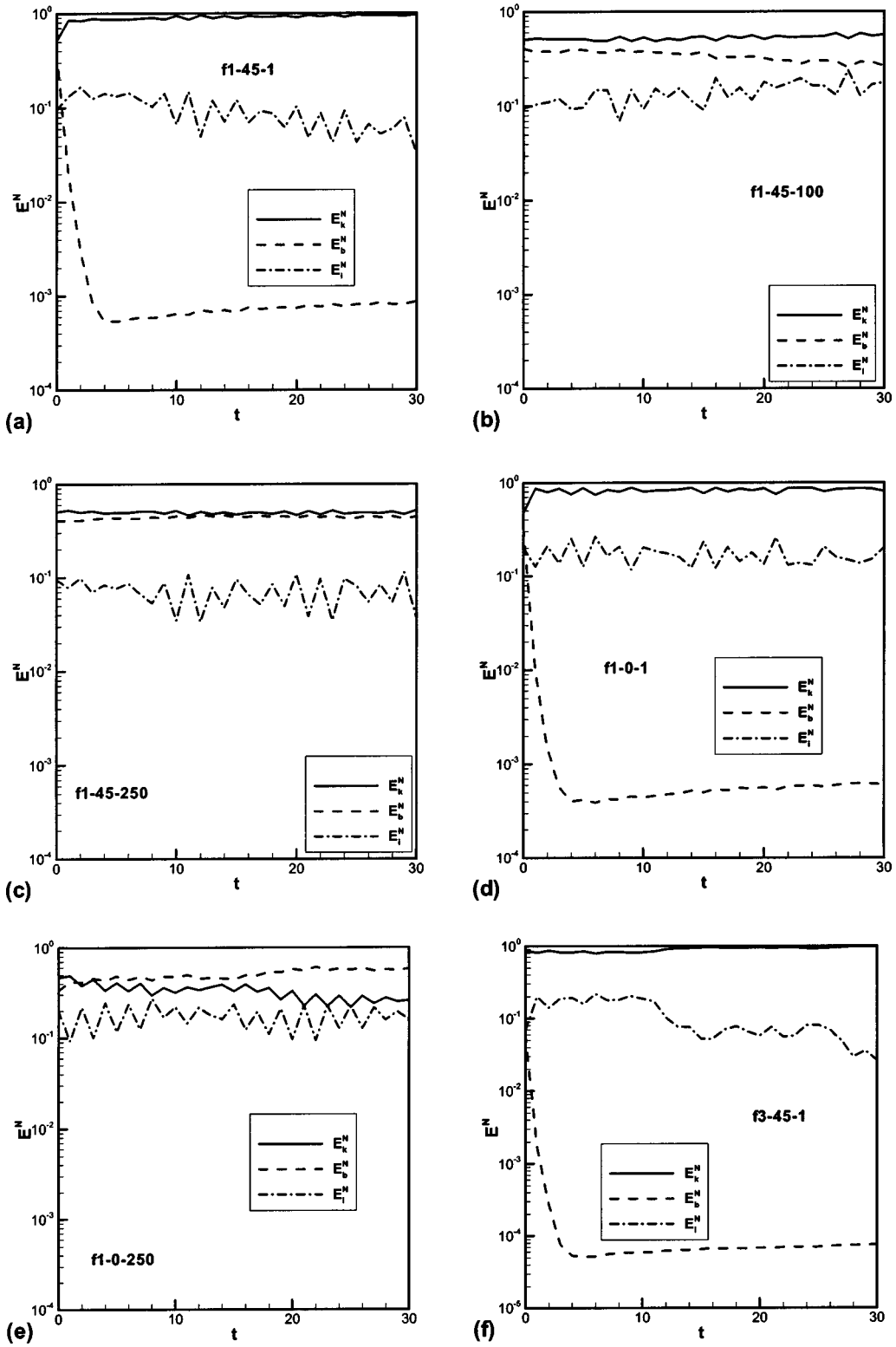

FIG. 13. Comparison of the fractional contribution of the three energy components for each MHD case study. Refer to the text and Table I for the various cases defined by the legend.

terms, the primitive variables are first differentiated and properly combined with the transport coefficients to form the requisite combinations of first derivative terms. These gradients are then differentiated again with the same difference scheme. The physical boundary conditions are applied after each update of the interior solution vector. Filters are employed to numerically stabilize the compact differencing calculations, as discussed in detail by Gaitonde and Visbal.[36] Time advancement is based on the fourth-order, four-stage, Runge–Kutta method.

The WENO schemes[37] pertain to the differencing of the convective terms of the equations in a way that avoids dis-

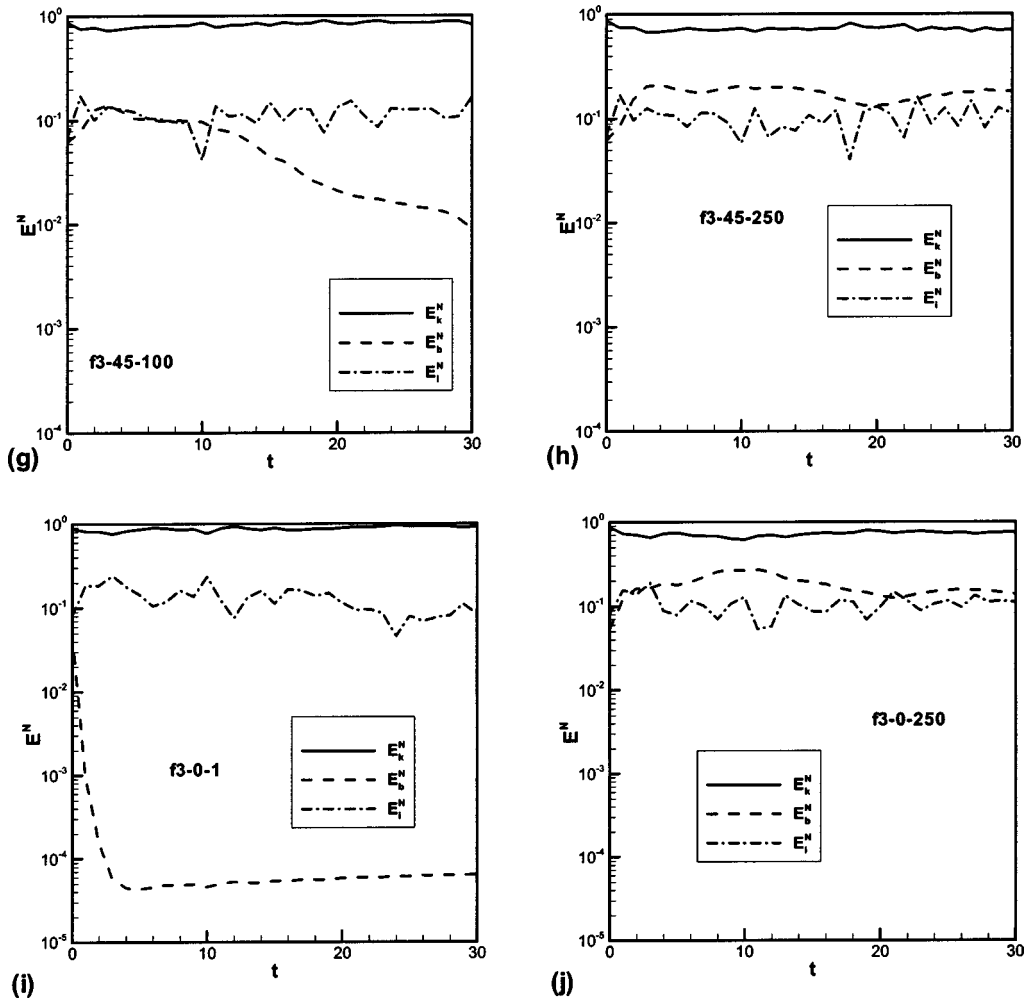

FIG. 13. (*Continued*.)

cretization across strong gradients. (The viscous terms are discretized with fourth order central schemes.) We can write the WENO problem for Eqs. (1)–(4) as

$$u_t(\xi,\eta,\zeta,t)+f_\xi(u(\xi,\eta,\zeta,t))+g_\eta(u(\xi,\eta,\zeta,t))+h_\zeta(u(\xi,\eta,\zeta,t))=0,$$

where u, f, g, and h are vector functions. The convective terms are reconstructed to accuracy k, which is taken as 6 in the present work. The basic WENO differencing problem is

$$\frac{du_{ijk}}{dt}=-\frac{1}{\Delta\xi}(\hat{f}_{i+(1/2),j,k}-\hat{f}_{i-(1/2),j,k})-\frac{1}{\Delta\eta}(\hat{g}_{i,j+(1/2),k}-\hat{g}_{i,j-(1/2),k})-\frac{1}{\Delta\zeta}(\hat{h}_{i,j,k+(1/2)}-\hat{h}_{i,j,k-(1/2)})$$
$$=f'+g'+h'+O(\Delta\xi^k,\Delta\eta^k,\Delta\zeta^k),$$
$$\equiv L(u),$$

where $\hat{f}$, $\hat{g}$, and $\hat{h}$ are high-order representations of the inviscid fluxes that are generated by the use of Lagrange interpolation. The reader is referred to Ref. 39 for the details of our implementation. The computational domain is a $2\pi\times2\pi$ periodic square. The reference length scale is the integral scales which, for the present work, could allow up to four energetic eddies in a direction of the computational box. The largest grid size that can be used to resolve the smallest scale of flow was calculated using standard procedures, such as on page 347 of the text by Pope.[42] According to this calculation, 128 spectral modes are sufficient in each direction. Preliminary calculations with resolutions of $512,^2$ $256,^2$ and 128^2 finite difference cells show that the scales of flow were resolved down to the Kolmogorov scale by all resolutions. Most of the calculations reported in this paper were carried out using $256.^2$ However, postprocessing the data for the plots was based on a 64^2 grid in order to reduce the computational cost which otherwise tends to be greater than that for the basic calculations. Using the reduced data sets in this manner did not introduce significant errors. Figures 1(a)–1(h) show the initial magnetic field arrow plots and the pressure contour maps for the cases f1-0-250, f1-45-250, f3-0-250, and f3-45-250 at $t=0$ and midway through the calculations, at $t=15$. Note that the magnetic field, as well as the velocity field (not shown) show approximately between 2 and 4 eddies in each direction of the box. The pressure contours show a much larger dimension for the structure because the total field ($\langle p\rangle+p'$) is shown. The displayed pressure

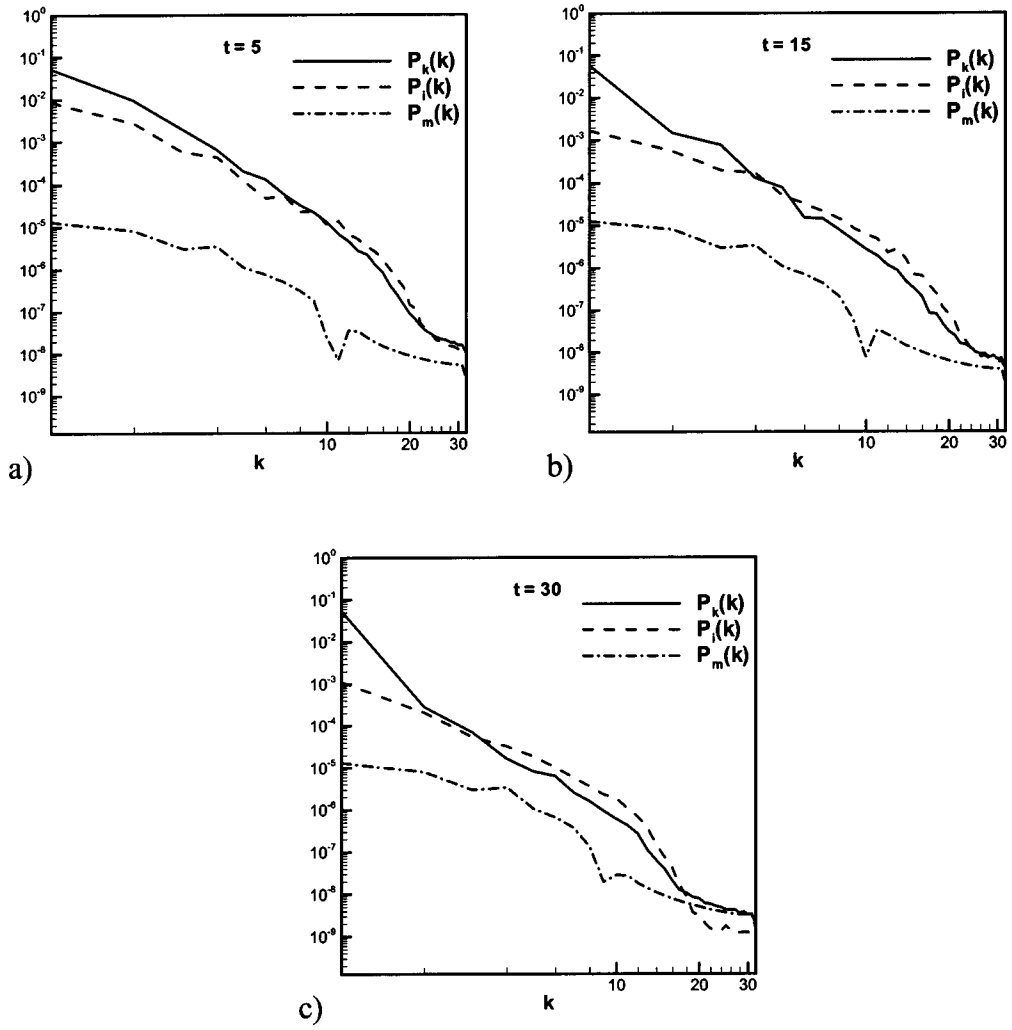

FIG. 14. Energy spectra at $t=5$, 15, and 30 for f3-45-1.

field is dominated by the underlying *mean* component which, depending on the particular initial condition [such as that in Fig. 1(c)], lacks a spectral distribution.

V. CASE STUDIES

The large number of parameters controlling the dynamics of the problem under investigation is evident. The calculations are limited to $M_a=0.5$. This choice is guided by the results in GM1 and from our own work,[35,40] in which the lower M_a calculations ($0.1\leqslant M_a\leqslant 0.3$) gave results that were similar to those of the corresponding incompressible cases, and higher M_a runs produced shocklets and other potentially discontinuous fields that require a different kind of analysis from the one presented in this paper. The effects of the initial hydrodynamic *turbulent* Reynolds number is also well known from previous work. This parameter is also kept fixed at a value of 250. The parameters k, μ, μ_m, and σ are set to unity, implying constant properties. The parameters varied in this study are, therefore, f_u, f_b, θ, and Re_σ. It is pointed out that the initial hydrodynamic Reynolds number, Re, is based on the root-mean squared turbulence velocity, u_{rms}, and a length scale of unity relative to the integral length scale. The value of 250 that is used in the present studies is bigger or at least comparable to those that have been used in many of the MHD studies we reviewed.[30–32,34] More importantly, for the target application (hypersonic flight), it is generally supposed that the turbulence intensity is low, so that the value of the turbulence Reynolds number used in the present study might be relevant to the real system.

Sixteen cases were investigated, as summarized in Tables I and II. They are referenced with two or three codes that are separated by hyphens; for example, f3-45-250. The first code roughly describes the relative intensity of the fluctuating velocity and magnetic induction fields, where f1 implies $f_b/f_u=1$ and f3 implies $f_b/f_u=3$. Note that f_u and f_b control the intensity of turbulence in the initial fields for **u** and **b**. The second code in this example, 45, denotes the value of the angle θ used in the correlation of the initial **u** and **b** fields, while the third code, for example 250, denotes the value of the magnetic Reynolds number, Re_σ. Cases XIII–XVII are non-MHD that have been included to assess the effects of MHD on the various results. These cases do not involve Re_σ. We investigated two values of θ: 0° and 45°. These lead to interesting initial correlations. Note that θ values of 30°, 60°, 120°, etc., give initial fields that are not

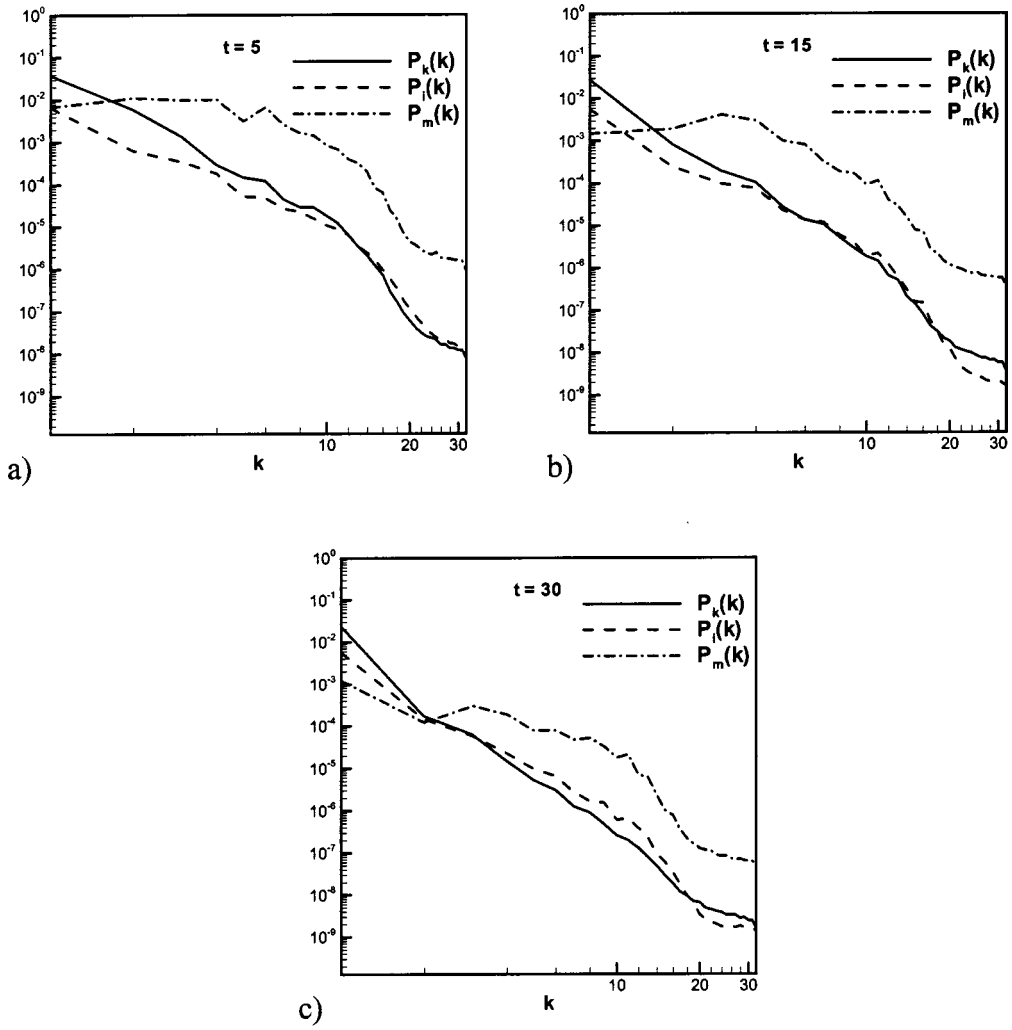

FIG. 15. Energy spectra at $t=5$, 15, and 30 for f3-45-100.

dynamically different. The choice of the values for f_u and f_b was based on a preliminary work that we carried out which showed that a field is complicated to calculate when b_{rms} is large. We also benefitted from discussions with Dr. S. Ghosh on this matter. Concerning the Re_σ values, we wanted a range that included low values, which are more relevant to aerospace applications, and values that are comparable to those that have been studied in previous work, to provide some basis for evaluating our calculations.

VI. RESULTS AND DISCUSSIONS

The computer program used for the present investigations has been thoroughly validated in order to engender confidence in the results it produces.[43,44] The basic compressible turbulence procedure, as well as the procedure to extract turbulence statistics have been validated by comparison of the results for various methods (ENO, WENO, compact schemes) to the pseudospectral calculations in GM1.[35,39,45] For the MHD simulation, we have compared predicted results using the program with analytical solutions for unsteady Alfvén waves with Ohmic damping.[41] A few of the results in this paper (e.g., the kinetic energy spectra) also agrees with those that use similar conditions in GM1.

Figures 2(a)–2(d) show the temporal evolution of the kinetic energy, $E_k(t)\equiv\langle\rho\mathbf{u}\cdot\mathbf{u}\rangle/2$ from the respective values of $E_k(0)=0.155$, 0.176, 0.778, and 0.928. The f1 case (for both $\theta=0°$ and $\theta=45°$) show identical evolution for $\mathrm{Re}_\sigma=1$ and non-MHD flows, Figs. 2(a) and 2(b), whereas, for f3, the non-MHD runs have a visibly faster decay rate. Note the difference in the scales of the graphs on the y-axis. This implies that the above difference in decay rates is significant and suggests that the effects of magnetic field on the evolution of the turbulence energy is negligible at the lowest magnetic Reynolds number investigated. The results also suggest that at the higher Re_σ values, when magnetic effects are important, the magnetic field tends to accelerate the decay of the turbulence energy relative to non-MHD flows. The nature of this enhancement in decay rate depends on the particular Re_σ values, the relative initial intensity of the **u** and **b** fields, and the correlation between the fields. For f3, the decay rate increases very rapidly with increasing Re_σ value, whereas the f1 cases show a nonmonotonic trend, with $\mathrm{Re}_\sigma=100$ decaying faster than $\mathrm{Re}_\sigma=250$. The reason for this peculiar behavior is not apparent, but we will return to this point later in the paper.

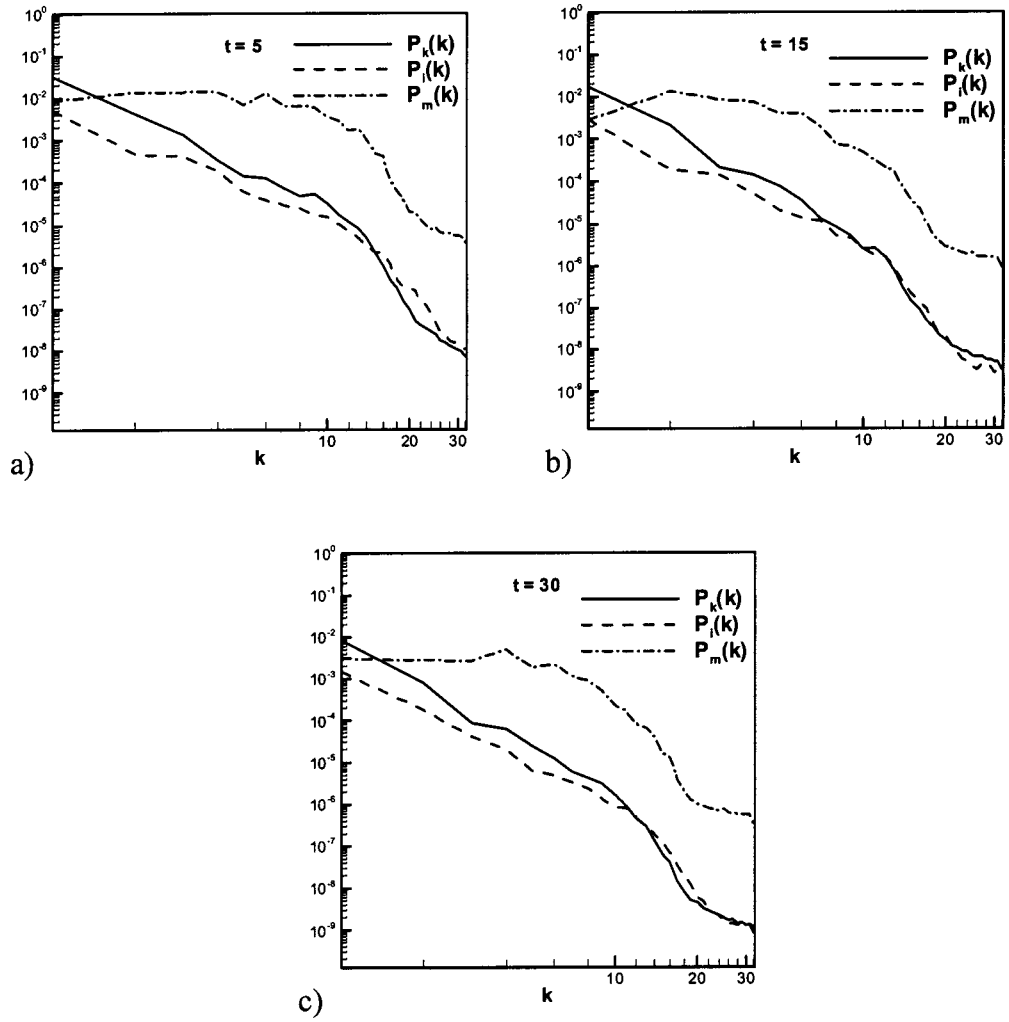

FIG. 16. Energy spectra at $t=5$, 15, and 30 for f3-45-250.

The foregoing trends for $E_k(t)$ are mirrored in the evolution of M_s^2 (Fig. 3), the instantaneous turbulence Reynolds number normalized by the initial u_{rms} value, Re, (Fig. 4), as well as the transverse component of the velocity field, U^T, which is calculated as

$$U^T=\langle\{|\mathrm{FFT}^{-1}(\hat{\mathbf{u}}^I)|^2\}\rangle^{1/2}.$$

The evolution of the longitudinal component, U^L, obtained by substituting $\hat{\mathbf{u}}^C$ for $\hat{\mathbf{u}}^I$ in this equation, is completely different from that for $E_k(t)$. Note that $\hat{\mathbf{u}}^C$ and $\hat{\mathbf{u}}^I$ are the spectral compressible and incompressible components of the velocity field, respectively. U^L shows an oscillatory pattern (Fig. 5), with magnitudes which are two to four times smaller than those for U^T (Fig. 6). This oscillation is expected if one considers that the compressible component usually propagates in waves.[35] The results for non-MHD and for $\mathrm{Re}_\sigma=1$ are relatively close, as has been observed above for other variables. With the exception of the f1-45 cases, which show continuous decay, the average (i.e., smoothened) profile (not explicitly shown) is characterized by an initial elevation with time, followed by a continuous decay. The profiles in Figs. 5(b)–5(d) appear to approach an equilibrium value of $U^L=0.1$, whereas the f1-45 cases approach $U^L=0.05$. The internal energy directly measures compressibility effects. Hence, the striking similarity in the evolution pattern for U^L and $E_i(t)$ (Fig. 7). Because of the relatively low Mach number, density fluctuations are small compared to the velocity fluctuations. Therefore, $M_s^2 \sim u_{\mathrm{rms}}^2$. Also, $E_k(t) \sim u_{\mathrm{rms}}^2$ and $\mathrm{Re} \sim u_{\mathrm{rms}}$ by their definitions. These scalings explain the similar trends observed for M_s^2, $E_k(t)$, and Re. The evolution of U^T (Fig. 6) is more difficult to explain. However, because the Mach number is not large, the incompressible component dominates the large scale velocity field; hence U^T scales with u_{rms} and the evolutionary trend for U^T should be similar to that for the other variables just discussed. On the other hand, $E_i(t)$ scales with the density fluctuation, and is therefore a direct measure of the extent of compressibility in the flow. Thus, the similar evolutionary trends for U^L and this quantity. Concerning Re evolution, the f1 cases appear to start from a value of 125 in the plots (Fig. 4), as opposed to the value of 250 that was imposed. For these cases, the specified Reynolds number, Re, is in fact equal to 250. However, the short time value of u_{rms} is approximately equal to 0.5, so that the effective (short time) Reynolds number is 125.0, which is what shows up in the

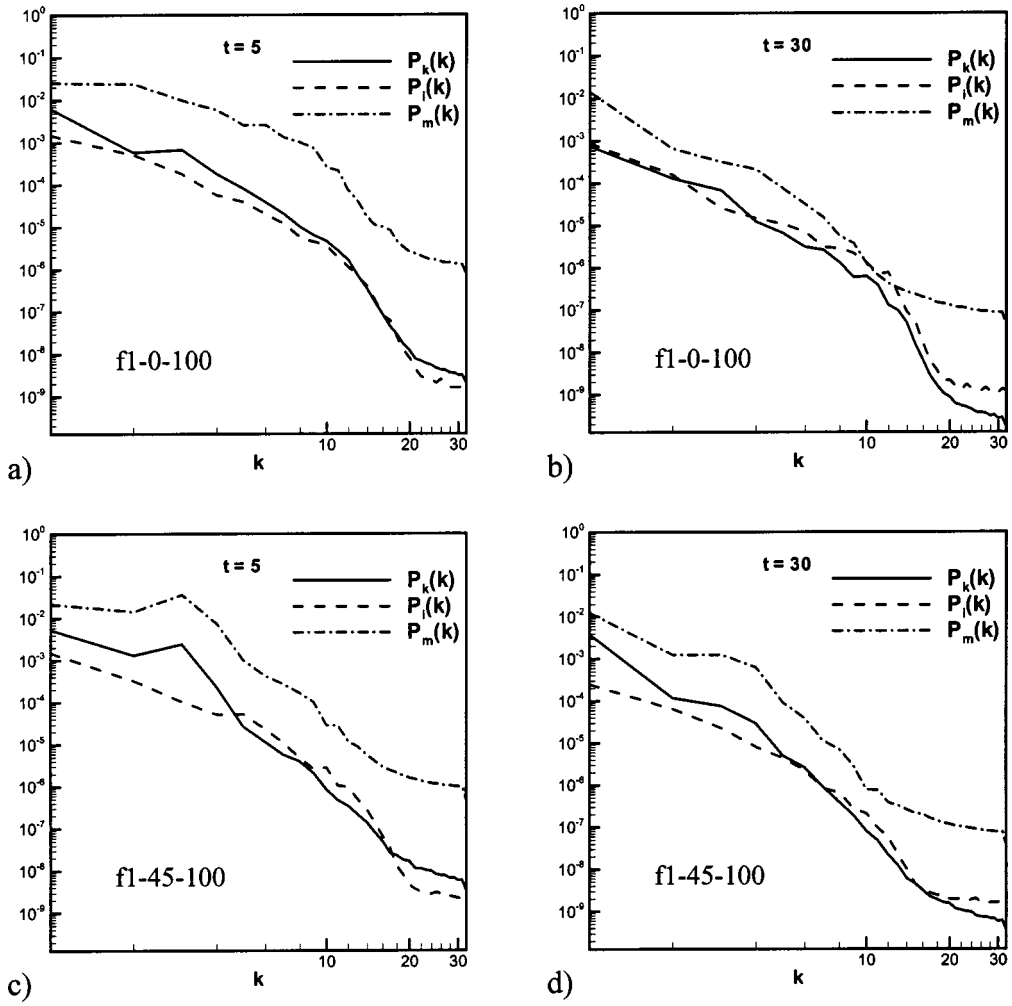

FIG. 17. Energy spectra at $t=5$ and 30 for f1-0-100 and f1-45-100.

plots. Because of this, some care is required when interpreting the results, although the general conclusions from the present studies remain unchanged. To have an effective Reynolds number of 250 at short time, the imposed value will have to be 500, which would still conflict with the value for the f3 cases, which is 250. [Note that $(u_{\mathrm{rms}})_{t\to 0}=1.0$ for the f3 cases.] Thus, the instant dip in the effective Re value for the f1 cases seems to be an unavoidable feature of the parameter space investigated.

The evolution pattern for the magnetic field energy, $E_b(t)\equiv R_b\langle \mathbf{b}\cdot\mathbf{b}\rangle/2\mu_m$, is quite different from that for the kinetic energy $E_k(t)$, even in simulations where the initial fluctuating **u** and **b** fields are similar (Fig. 8). In all cases investigated, when $\mathrm{Re}_\sigma=1$, this quantity is rapidly driven from its initial values (0.125 and 0.05556) to essentially zero. This result has not been reported in the literature, perhaps because most fundamental studies have focused on applications where Re_σ is two orders of magnitude larger ($\mathrm{Re}_\sigma=250$). In general, the cases with $\mathrm{Re}_\sigma=250$ show weaker decay rates than do the cases with $\mathrm{Re}_\sigma=100$. For f1 and $\theta=45°$, the magnetic energy decays continuously with time from its initial value of 0.125. When $\theta=0°$, the f1 cases show a rapid jump of the magnetic energy from 0.125 to 0.14 before beginning a continuous, nonlinear decay with time. The initial jump occurs earlier than $t=1$. The f3 calculations for both θ values also show a similar trend, with the jump occurring at a slightly later time ($t=4$ for f3-45-250 and $t=2$ for f1-0-250). An important conclusion from Fig. 8 is that higher Re_σ values significantly slow down the magnetic energy decay rates, thereby prolonging the time it takes for the magnetic energy to die off completely. At the lowest Re_σ value investigated, the magnetic energy decays to zero almost instantly. Note also that the E_b decay mode is less sensitive to the initial correlation angle θ, in comparison to the decay rate of E_k.

Figures 9–12 and Table III show the decomposition of the total energy, $E_t\equiv E_k+E_b+E_i$ into its normalized components E_k^N, E_b^N, and E_i^N. Note that Figs. 9–12 are grouped in a way that allows easy assessment of the effects of magnetic Reynolds number. Figure 13 contains the same information, but the plots are organized to allow easy comparison of the evolution pattern of the energy components for each case. We see in Fig. 9 that with normalization, a monotonic effect of Re_σ on the kinetic energy can be observed, thereby showing a consistent Re_σ effect on the kinetic energy across the various cases investigated. It can also be observed that during most of the transient, the percent contribution (E_k^N) of E_k

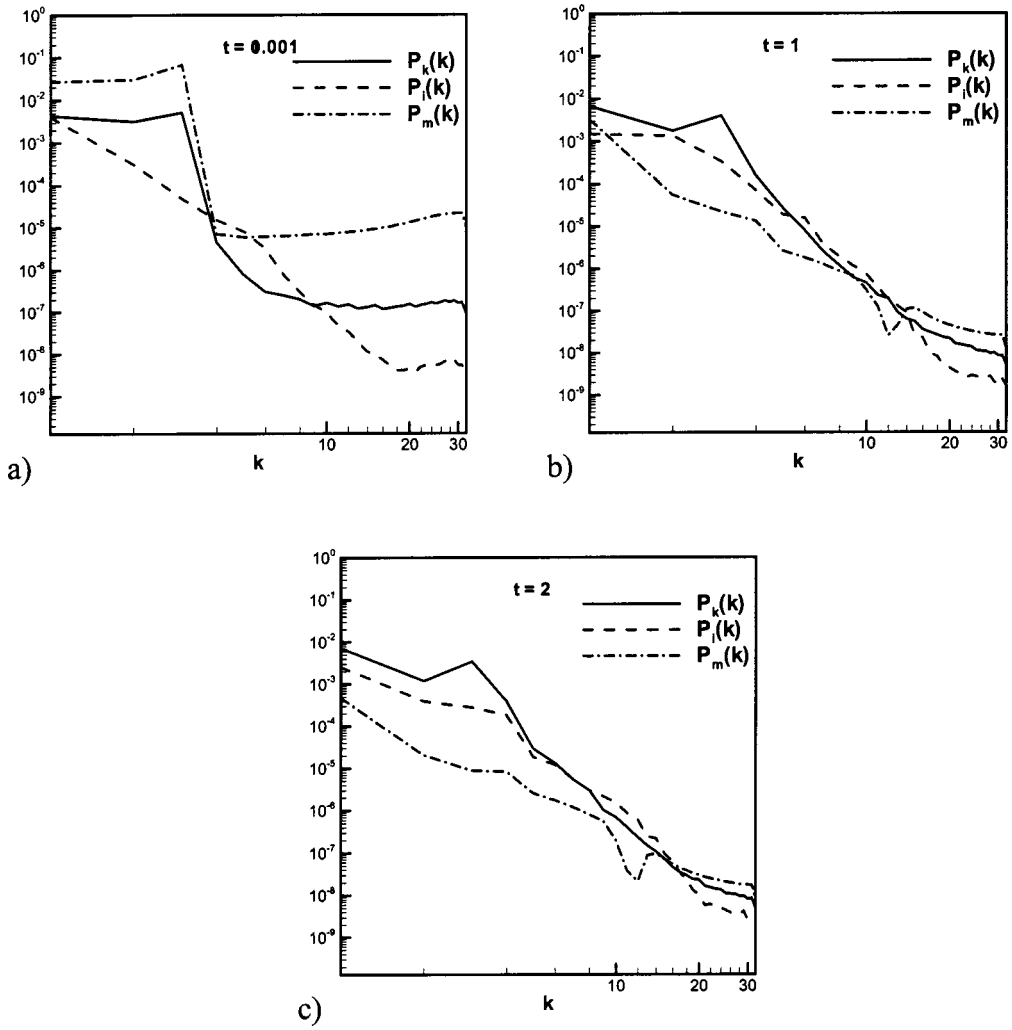

FIG. 18. Energy spectra at $t=0.001$, 1.0, and 2.0 for f1-45-1.

to E_t decreases with increasing Re_σ (Fig. 9) while that of E_b shows the opposite trend (Fig. 10). Hence, and as Fig. 11 and Table III show, the intermediate Re_σ calculations (i.e., $\mathrm{Re}_\sigma=100$) appear to give the largest contribution of the internal energy E_i to the total energy. This suggests an interaction between Re_σ and the level of density fluctuation (or compressibility) in the flow. The data also show that, for the same θ and Re_σ, the f3 cases lead to a relatively high contribution of E_k compared to the f1 cases, whereas f3 leads to a weaker contribution of E_b. Note that E_t decreases with increasing Re_σ (Fig. 12), except for the f1-45 cases, where the E_t for the three Re_σ calculations are of comparable order but do not show a definite trend. The E_i enhancement at $\mathrm{Re}_\sigma=100$ (see comments below) seems to be responsible for this observation. For f1-0, E_t decreases with Re_σ by a factor of over 2, whereas for f3-45 and f3-0 the ratio is over 3 and 7, respectively. Hence, the relative initial intensity of the flow and magnetic fields determines the dependence on Re_σ.

The spectra of the kinetic energy, $P_k(\kappa)$, internal energy, $P_i(\kappa)$, and magnetic energy, $P_m(\kappa)$, are shown in Figs. 14–19. Some general observations can made, such as the absence of a large scale region where the energy increases with the wave number, κ, as in the familiar κ^{+2} profile.[42] Thus, the energy decreases continuously downscale, in an approximately monotonic fashion, although with some exceptions in the P_m profile when $\mathrm{Re}_\sigma=1$. The observations for higher Re_σ cases are similar to those in GM1. At low wave numbers, the tendency is for larger spectral energy with decreasing Re_σ. However, the spectral decay rate with Re_σ tends to go in the opposite direction, at the large to intermediate scales (low to intermediate κ values): the higher Re_σ cases tend to contain more energy. The results show that the f3 cases contain more energy at the large scales compared to the f1 cases. Thus, the initial relative intensity of the **u** and **b** fluctuations affect the partitioning of the energy into the spectral modes. The relative contribution of the three energy modes can also be observed in the spectra. (The kink in the P_m profile around $t=10$ when $\mathrm{Re}_\sigma=1$ is discussed below.) That is, at the low and intermediate wave numbers, $P_m(k)$ has significantly smaller amplitudes compared to $P_k(k)$ or $P_i(k)$ (Fig. 14), whereas it has a significant contribution at the larger Re_σ values (Figs. 15 and 16). Concerning $P_k(k)$ and $P_i(k)$, the internal energy becomes increasingly significant relative to the kinetic energy, as the high wave number end of the spectrum is approached, such that the two are approximately equipartitioned. This is consistent with the results in GM1.

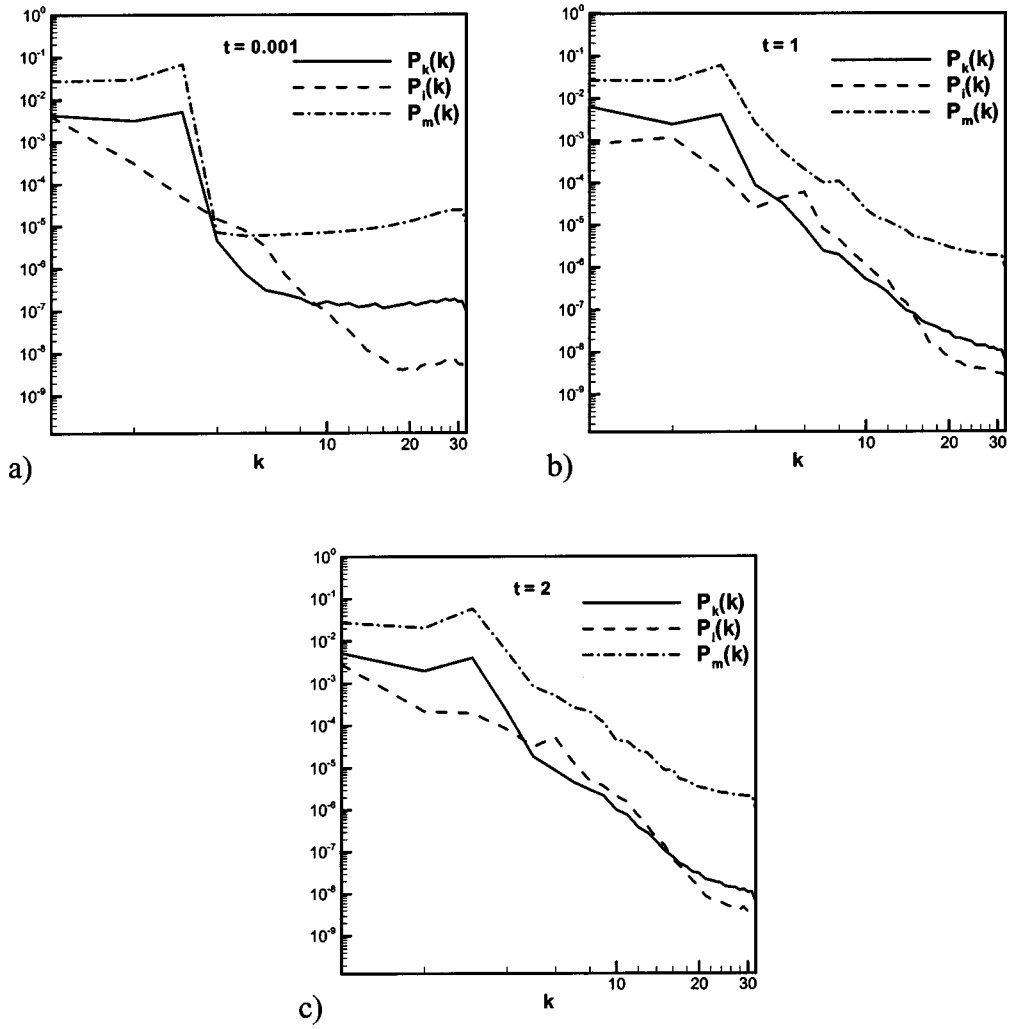

FIG. 19. Energy spectra at $t=0.001$, 1.0, and 2.0 for f1-45-250.

Re_σ does not affect the initial conditions. However, as time advances, and at the low wave number end of the spectra, the intermediate Re_σ calculations show significant levels of internal energy relative to the kinetic energy (Fig. 15). That is, the difference between $P_k(k)$ and $P_i(k)$ at the low wave numbers, where the amplitudes are significant, is smallest when $\mathrm{Re}_\sigma=100$, and decreases even further with time. Note that this effect is more pronounced for the f3-45 case (Fig. 15) compared to the f1-45 case (Fig. 17). The slow relaxation (or the persistence) of the imposed kinetic energy in the f1-45 case seems to be responsible for the difference. While the real reason for this relaxation behavior is not entirely clear, it may be due to lower amplification (decay) rates that are usually associated with small amplitudes, from the view point of hydrodynamic stability.[40] (See Table II, cases III and VIII for the initial kinetic energy levels.) Note that, whereas Fig. 11 (or Table III) shows the most enhancement of the internal energy mode by f1-0-100, followed by f1-45-100, the spectra plots in Figs. 15 and 17 show that the case f3-45-100 has higher levels of internal energy. These two sets of data cannot really be compared because, whereas the data in Fig. 11 are one-point, having been obtained as spatially averaged values, those in Figs. 15 and 17 are for the spectra at the specified time steps.

Figures 18 and 19 have been provided to explain the nonmonotonic (kink) behavior in the $P_m(k)$ profile when $\mathrm{Re}_\sigma=1$. The figures show the short time behavior ($t=0.001$, 1, and 2). The spectra at $t=0.001$ are clearly those of the initial tophat profile in $1\leqslant k\leqslant\sqrt{12}$. Note that the internal energy spectra do not have the tophat shape because the initial density field was not filtered with this distribution. In any case, the kinetic energy spectra relax into fairly monotonic distributions early in the transient ($t=1$). The same is true for the magnetic energy spectra when $\mathrm{Re}_\sigma=100$ or 250 (Fig. 19). For the $\mathrm{Re}_\sigma=1$ case, it appears that a remnant of the tophat profile in $P_m(k)$ is transported downscale (i.e., to the high wave number end of the spectrum) as time progresses, rather than being ''smeared,'' leading to the kink in the $P_m(k)$ profile at this Re_σ value.

Figures 20(a)–20(d) are typical spectra of U^T and U^L for f1-45-1 [(a) and (b)] and f3-45-1 [(c) and (d)] at two instants ($t=5,30$) during the relaxation process. The effects of Re_σ on these quantities (not shown) are not as strong as on the respective energies, again suggesting significant interaction

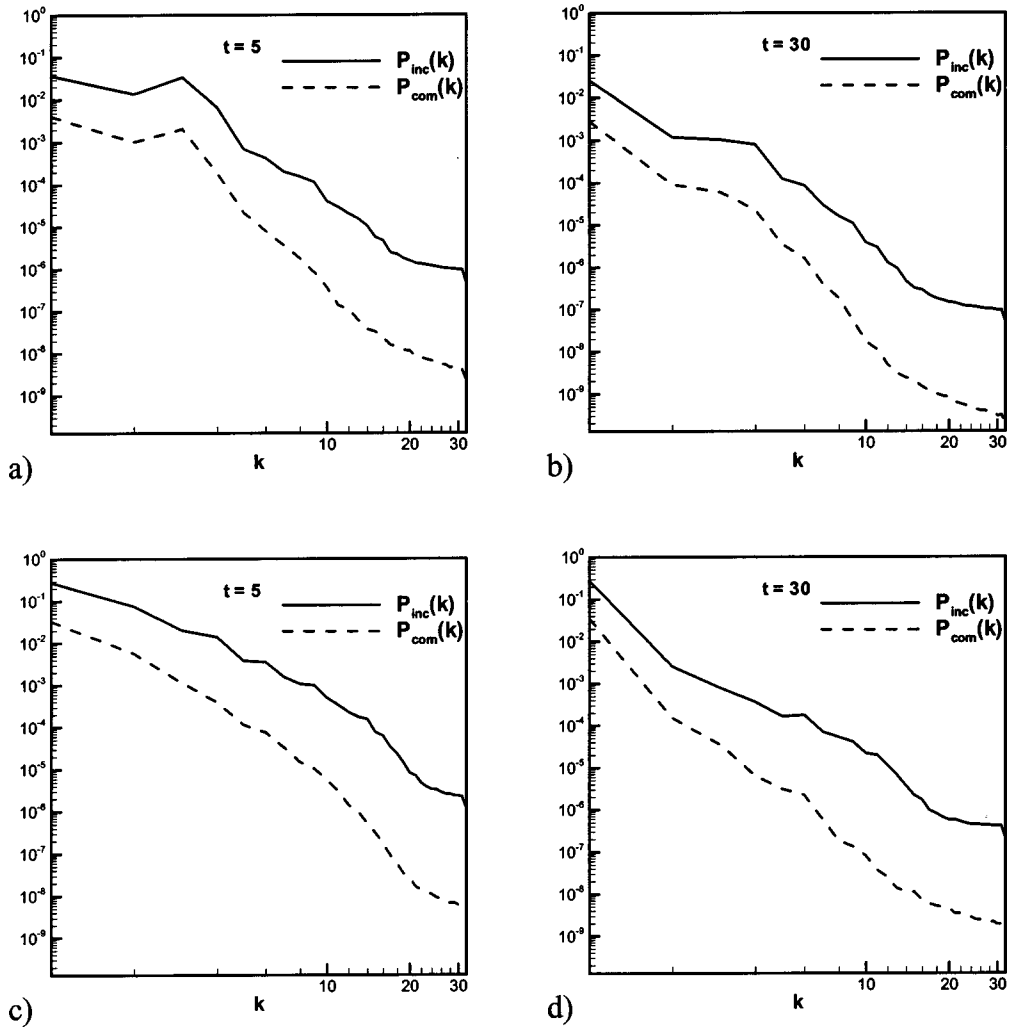

FIG. 20. Spectra of $U^T(P_{\text{inc}}(k))$ and $U^L(P_{\text{com}}(k))$ at $t=5$ and 30 for f1-45-1 (a,b) and f3-45-1 (c,d).

between density ρ and the magnetic Reynolds number Re_σ. Finally, as mentioned in GM1, it is difficult, and probably inappropriate, to assign a steady inertial spectral index to the computed spectra because of ongoing nonlinear development and limited bandwidth.

Figures 21(a)–21(d) describe the evolution of the cross correlation, R_{ub}:

$$R_{ub}=\frac{\langle \mathbf{u}\cdot\mathbf{b}\rangle}{\{\langle|\mathbf{u}|^2\rangle\langle|\mathbf{b}|^2\rangle\}^{1/2}}$$

for cases I–XII in Tables I and II. R_{ub} represents the normalized cross correlation (cross helicity) between the **u** and **b** fields. That is, an indicator of whether these fields increase or decrease together, or a decrease in one field is accompanied by an increase in the other. In the initial field, θ determines this correlation, as discussed earlier in this paper. Whether an initially high correlation remains high depends on the initial relative intensities of the two fields. What we see in Fig. 21 is that $\theta=0°$ not only gives a low correlation at the initial time but that the correlation remains weak during the evolution of the flow. When $\theta=0°$ and the initial intensities of the fields are comparable (i.e., f1-0-1, f1-0-100, and f1-0-250), the small correlation there is at the initial instant goes to zero with time, monotonically for $\text{Re}_\sigma=250$ but in an oscillatory fashion for $\text{Re}_\sigma=1$ [Fig. 21(b)]. The tendency toward negative correlation (with time evolution) as observed for f1-0-250 is not present for f3-0-250.

The R_{ub} results for $\theta=45°$ are significantly different from those for $\theta=0°$, the most pronounced being in the results for $\text{Re}_\sigma=1$, for both f1 and f3. For this case (i.e., $\theta=45°$), when $\text{Re}_\sigma=1$, R_{ub} drops off rapidly from its initial value of around 1.0, to zero at approximately $t=0.5$ (f1) and $t=0.4$ (f3). At the higher Re_σ values ($\text{Re}_\sigma=100,250$), the unity value of R_{ub} is maintained for f1-45. For f3-45, it drops to between 0.4 and 0.75.

In summary, the most dramatic results for R_{ub} pertain to the fast decay to zero of the correlation when $\text{Re}_\sigma=1$, independent of the initial correlations and the initial relative intensities of the flow and magnetic fields. That is, the two fields tend to be uncorrelated when the magnetic Reynolds number is low. By virtue of the homogeneous nature of the flow and magnetic fields, we can conclude that the fields are also statistically independent at the lowest Re_σ value investigated, since $\langle \mathbf{u}\cdot\mathbf{b}\rangle \approx \langle \mathbf{u}\rangle\langle \mathbf{b}\rangle \approx \mathbf{0.0}$. In this case, the role of the magnetic field is passive, and it is merely convected by the velocity field. In nonhomogeneous velocity and magnetic

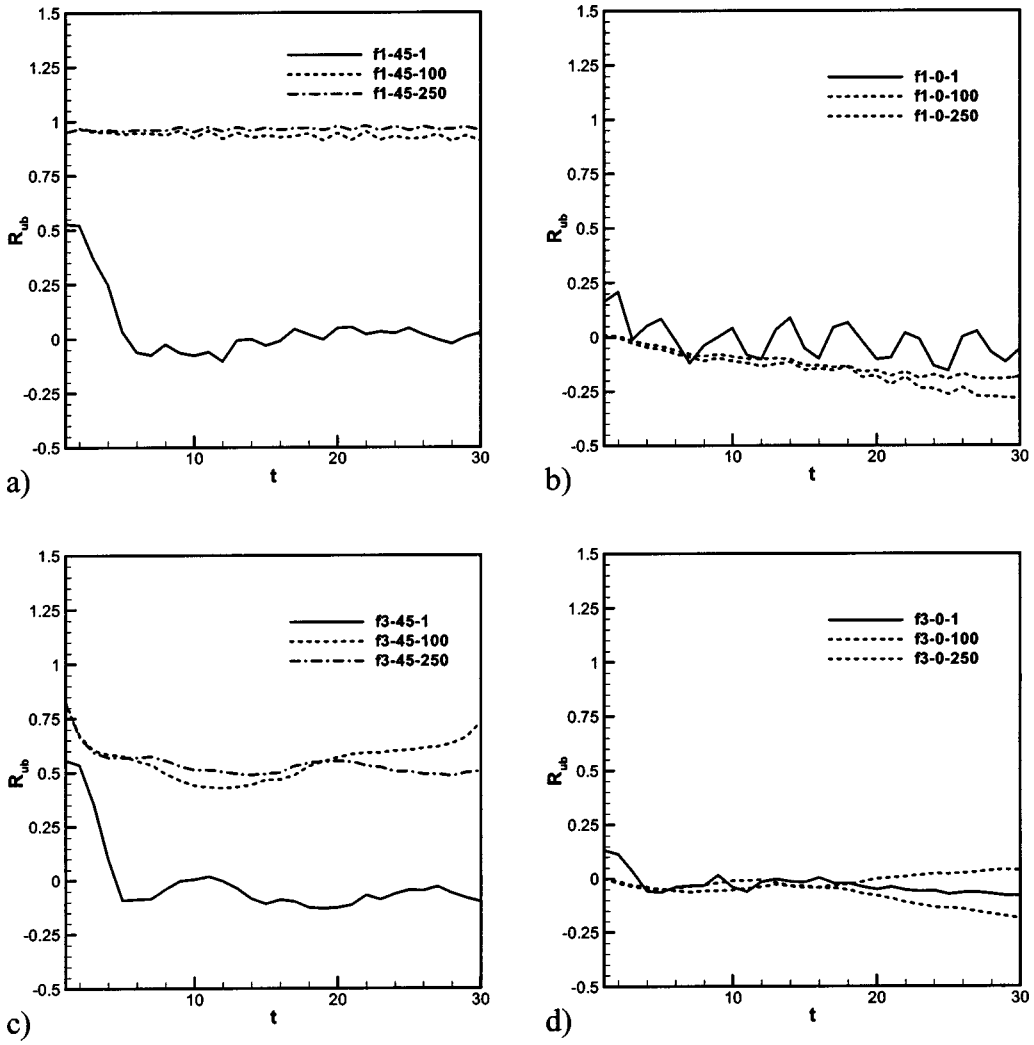

FIG. 21. Evolution of the normalized cross helicity, R_{ub}. Refer to the text and Table I for the various cases defined by the legend.

fields, the two fields are more likely to be statistically dependent, even if they are uncorrelated and $\mathrm{Re}_\sigma=1$. Note that to maintain a high correlation of the fields during evolution, we need to have a high correlation in the initial field and the initial relative intensity of the fluctuations must be comparable, as in the f1 cases. The Re_σ values must also be large within the range used in this paper.

The fast temporal decay of the magnetic energy E_b for $\mathrm{Re}_\sigma \to 0$ can be explained if we consider the linearized system

$$\frac{\partial b_i}{\partial t} = B_{oj} u_{i,j} + \frac{1}{\mathrm{Re}_\sigma} \Delta b_i .$$

In Fourier space, this equation has the solution

$$b_i(\mathbf{k},t) = b_i(\mathbf{k},0) e^{-(k^2/\mathrm{Re}_\sigma)t} + i \int_0^t d\tau k_j B_{oj} u_i(\mathbf{k},\tau) \times e^{-(k^2/\mathrm{Re}_\sigma)(t-\tau)},$$

which shows a rapid decay of $\mathbf{b}$ (and E_b) with time for small values of Re_σ, as predicted by the DNS calculations. This is another demonstration that our calculations are probably very accurate. Note that the existence or otherwise of a mean field $\mathbf{B}_0$ does not affect this conclusion.

The rapid decay of R_{ub} when $\mathrm{Re}_\sigma \to 0$ can also be explained, as follows. As the figures show, the $\mathbf{b}$ field decays rapidly to attain essentially constant values after the initial transient. On the other hand, the $\mathbf{u}$ field continues to decrease with time. Hence, the two fields are uncorrelated, so that $\langle \mathbf{u} \cdot \mathbf{b} \rangle = \mathbf{0}$, as in the DNS results.

It is pointed out that the present DNS results for $\mathrm{Re}_\sigma = 1$ can be used to assess the accuracy of both the quasistatic[22] and the quasilinear[34] approximations. These simplifications have been studied for incompressible flows; the present results can be used to investigate their validity for compressible flows.[13] Note that the quasistatic model may not be appropriate for investigating decaying turbulence because of the crucial dependence of the evolution on the initial conditions. A modally forced calculation might be more acceptable in a DNS work that uses the quasistatic approximation, as in Zikanov and Thess.[11] The quasilinear model is more acceptable is this regard, as long as Re_σ is very small.

VII. CONCLUDING REMARKS

We have carried out direct simulation of MHD turbulence in this paper for the purpose of investigating the effects of the magnetic Reynolds number. Most previous fundamental works on the subject have used conditions or assumptions, such as the quasistatic approximations, incompressibility, large values of the magnetic Reynolds number, the Orszag–Tang initial conditions, and spectral forcing, that make them inappropriate for our interest. We study the effects of magnetic Reynolds number in compressible simulations that use the full MHD formulation. The initial fields are carefully determined, with particular emphasis on the relative intensities of the fluctuating velocity and magnetic fields and the initial cross helicity. The study that most closely relates to the present one is GM1. We used the results in GM1 to validate our procedure, which differs significantly from that in GM1. However, the details of the initial conditions and the parameter ranges investigated in the present paper are completely different from those in GM1. Therefore, the details of the results we present in this paper cannot be compared directly to those in GM1. There are some qualitative agreements in the few cases where the parameters are of comparable *order* of magnitude.

To our knowledge, some of the results reported in this paper are new. The studies suggest that the effects of magnetic field on the evolution of the turbulence energy is negligible at the lowest magnetic Reynolds number investigated and that at the higher Re_σ values, when magnetic effects are important, the magnetic field tends to accelerate the decay of the turbulence energy relative to non-MHD flows. The nature of this enhancement in decay rate depends on the particular Re_σ values, the relative initial intensity of the **u** and **b** fields, and the initial correlation between the fields. We have observed a similar evolution pattern for the quantities M_s^2, Re, $E_k(t)$, and U^T and for E_i and U^L, and have provided an explanation for the observation. In all cases investigated, when $\mathrm{Re}_\sigma=1$, the magnetic energy is rapidly driven from its initial values to essentially a value of zero very early in the transient. Higher Re_σ values significantly slow down the magnetic energy decay rates. We have also seen that the E_b decay mode is less sensitive to the initial correlation between the velocity and magnetic fields, in comparison to the decay rate of E_k. During most of the transient, the percent contribution (E_k^N) of E_k to the total energy E_t decreases with increasing Re_σ, while that of E_b shows the opposite trend. The intermediate Re_σ calculations (i.e., $\mathrm{Re}_\sigma=100$) appear to give the largest contribution of the internal energy E_i to the total energy. This suggests an interaction between Re_σ and the level of the density fluctuations (or compressibility) in the flow. Note that E_t decreases with increasing Re_σ, except for the f1-45 cases, where the E_t for the three Re_σ calculations are of comparable order and do not show a definite trend. The E_i enhancement at $\mathrm{Re}_\sigma=100$ seems to be responsible for the deviation for the f1-45 cases. The initial relative intensity of the **u** and **b** fluctuations affect the partitioning of the energy into the spectral modes.

The relative role of the internal energy at $\mathrm{Re}_\sigma=100$ does not appear to be random, since it is fairly consistent across the majority of cases investigated. A spectral plot also supports the unexpected behavior, and calculations were repeated to confirm the observations. A precise explanation is not available at the moment, although we are currently studying the energy exchange dynamics between kinetic, magnetic, and internal components. The procedure followed is conceptually similar to that in Tennekes and Lumley[46] for the role of pressure strain in energy exchange. The details are different, however. Because the exercise is a major one, involving both theoretical and parametric studies with different values of Re_σ, f_u, f_b, etc., the results from it are not available for the present paper.

An interesting result for R_{ub} pertains to the fast decay to zero of this quantity when $\mathrm{Re}_\sigma=1$, independent of the initial correlations and the initial relative intensities of the flow and magnetic fields. That is, the two fields tend to be uncorrelated when the magnetic Reynolds number is low so that they are statistically independent at this Re_σ value. In this case, the role of the magnetic field is passive, and is merely convected by the velocity field. Note that, to maintain a high a correlation between the fields during evolution, the correlation must be high in the initial field and the initial relative intensity of the fluctuations must be comparable. The Re_σ values must also be large (within the range used in this paper) for the fields to be correlated.

ACKNOWLEDGMENTS

This work was partially supported by the National Research Council (NRC) Summer Faculty Program and the Air Vehicles Directorate of the Air Force Research Laboratory at Wright–Patterson Air Force Base, Dayton, OH. The contribution of our colleagues Dr. Stavros Kassinos and Dr. X. Cai is gratefully acknowledged. The first author (F.L.) would like to express his appreciation to Dr. Sanjoy Ghosh for the numerous discussions during the course of this work. Some of the calculations would have been more difficult to perform, if not impossible, without the hints provided by Dr. Ghosh. Vivian Shao helped with the plots.

[1] J. B. Taylor, "Relaxation of toroidal plasma and generation of reverse magnetic field," Phys. Rev. Lett. **33**, 1139 (1974).
[2] J. B. Taylor, *Pulsed, High-Beta Plasmas*, edited by D. E. Evans (Pergamon, Oxford, 1976), pp. 59–67.
[3] D. Montgomery, L. Turner, and G. Vahala, "Three-dimensional magnetohydrodynamic turbulence in cylindrical geometry," Phys. Fluids **21**, 757 (1978).
[4] A. C. Ting, W. H. Matthaeus, and D. Montgomery, "Turbulent relaxation processes in magnetohydrodynamics," Phys. Fluids **29**, 3261 (1986).
[5] R. V. E. Lovelace, "Dynamo model of double radio sources," Nature (London) **262**, 649 (1976).
[6] R. V. E. Lovelace, C. Mahanian, C. M. Mobarry, and M. E. Sulkanen, "Theory of axisymmetric magnetohydrodynamic flows: Disks," Astrophys. J., Suppl. Ser. **62**, 1 (1986).
[7] R. V. E. Lovelace, J. C. L. Wang, and M. E. Sulkanen, "Self-collimated electromagnetic jets from magnetized accretion disks," Astrophys. J. **315**, 504 (1987).
[8] J. Heyvaerts, E. R. Priest, and D. M. Rust, "An emerging flux model for the solar flare phenomenon," Astrophys. J. **216**, 123 (1977).
[9] R. Grappin, A. Pouquet, and J. Léorat, "Dependence of MHD turbulence spectra on the velocity field–magnetic field correlation," Astron. Astrophys. **126**, 51 (1983).
[10] R. B. Dahlburg, J. P. Dahlburg, and J. T. Mariska, "Dependence of MHD

turbulence spectra on the velocity field-magnetic field correlation,'' Astron. Astrophys. **198**, 300 (1988).
[11]O. Zikanov and A. Thess, ''Direct numerical simulation of forced MHD turbulence at low magnetic Reynolds number,'' J. Fluid Mech. **358**, 299 (1998).
[12]F. Ladeinde, ''Direct simulation of MHD turbulence,'' AIAA 2002-2140, 33rd AIAA Plasmadynamics and Laser Conference, 20–23 May 2002, Maui, HI.
[13]F. Ladeinde and D. V. Gaitonde, ''An evaluation of the quasi-static formulation for compressible magnetogasdynamic turbulence,'' AIAA 2003-3481, 34rd AIAA Plasmadynamics and Laser Conference, 23–26 June 2003, Orlando, FL.
[14]R. W. Ziemer and W. B. Bush, ''Magnetic field effects on bow shock stand-off distance,'' Phys. Rev. Lett. **1**, 58 (1958).
[15]R. X. Meyer, ''Magnetohydrodynamics and aerodynamic heating,'' ARS J. **29**, 187 (1959).
[16]D. C. Robinson and M. G. Rusbridge, ''Structure of turbulence in the zeta plasma,'' Phys. Fluids **14**, 2499 (1971).
[17]S. J. Zweben, C. P. Menyuk, and R. J. Taylor, ''Small-scale magnetic fluctuations inside the macrotor tokamak,'' Phys. Rev. Lett. **42**, 1270 (1979).
[18]H. K. Moffatt, ''On the suppression of turbulence by a uniform magnetic field,'' J. Fluid Mech. **23**, 571 (1967).
[19]J. Sommeria and R. Moreau, ''Why, how, and when, MHD turbulence becomes two-dimensional,'' J. Fluid Mech. **118**, 507 (1982).
[20]P. A. Davidson, ''Magnetic damping of jets and vortices,'' J. Fluid Mech. **299**, 153 (1995).
[21]P. A. Davidson, ''The role of angular momentum in the magnetic damping of turbulence,'' J. Fluid Mech. **336**, 123 (1997).
[22]P. H. Roberts, *An Introduction to Magnetohydrodynamics* (American Elsevier, New York, 1967).
[23]U. Frisch, A. Pouquet, J. Léorat, and A. Mazure, ''Possibility of inverse cascade of magnetic helicity in magnetohydrodynamic turbulence,'' J. Fluid Mech. **68**, 769 (1975).
[24]A. Pouquet and G. S. Patterson, ''Numerical simulation of helical magnetohydrodynamic turbulence,'' J. Fluid Mech. **85**, 305 (1978).
[25]T. Gomez, H. Politano, and A. Pouquet, ''On the validity of a nonlocal approach for MHD turbulence,'' Phys. Fluids **11**, 2298 (1999).
[26]R. H. Kraichnan, ''Inertial range spectrum of hydrodynamic turbulence,'' Phys. Fluids **8**, 1385 (1965).
[27]P. Iroshnikov, ''Turbulence for a conducting fluid in a strong magnetic field,'' Sov. Astron. **7**, 566 (1963).
[28]W.-C. Muller and D. Biskamp, ''Scaling properties of three-dimensional magnetohydrodynamic turbulence,'' Phys. Rev. Lett. **84**, 475 (2000).
[29]S. Orszag and C.-M. Tang, ''Small-scale structure of two-dimensional magnetohydrodynamics,'' J. Fluid Mech. **90**, 129 (1979).
[30]R. B. Dahlburg and J. M. Picone, ''Evolution of the Orszag–Tang vortex system in a compressible medium. I. Initial average subsonic flow,'' Phys. Fluids B **1**, 2153 (1989).
[31]J. M. Picone and R. B. Dahlburg, ''Evolution of the Orszag–Tang vortex system in a compressible medium. II. Supersonic flow,'' Phys. Fluids B **3**, 29 (1991).
[32]S. Ghosh and W. H. Matthaeus, ''Relaxation processes in a turbulent compressible magnetofluid,'' Phys. Fluids B **2**, 1520 (1990).
[33]M. P. Martin and G. V. Candler, ''Effect of chemical reactions on decaying isotropic turbulence,'' Phys. Fluids **10**, 1715 (1998).
[34]S. C. Kassinos, B. Knaepen, and D. Carati, ''MHD turbulence in the presence of a strong magnetic field,'' in Proceedings of the Summer Program 2002, Center for Turbulence Research, Stanford University/NASA Ames Research Center, 2002.
[35]F. Ladeinde, E. E. O'Brien, X. D. Cai, and W. Liu, ''Advection by polytropic compressible turbulence,'' Phys. Fluids **7**, 2848 (1995).
[36]D. V. Gaitonde and M. R. Visbal, ''High-order schemes for Navier–Stokes equations: Algorithm and implementation into FDL3DI,'' Technical Report No. AFRL-VA-WP-TR-1998-3060, Air Force Research Laboratory, Wright-Patterson AFB, OH, 1999.
[37]C.-W. Shu, ''Essentially non-oscillatory and weighted essentially non-oscillatory schemes for hyperbolic conservation laws,'' ICASE Report No. 97–65 (1997).
[38]M. R. Visbal and D. V. Gaitonde, ''On the use of higher-order finite difference schemes on curvilinear and deforming meshes,'' J. Comput. Phys. **181**, 155 (2002).
[39]F. Ladeinde, X. Cai, M. R. Visbal, and D. V. Gaitonde, ''Turbulence spectra characteristics of high order schemes for direct and large eddy simulation,'' Appl. Numer. Math. **36**, 447 (2001).
[40]F. Ladeinde and J. Wu, ''Second order nonlinear spatial stability analysis of compressible mixing layers,'' Phys. Fluids **14**, 2968 (2002).
[41]D. V. Gaitonde and J. Poggie, ''Preliminary analysis of 3D scram jet flow path with MGD control,'' AIAA 2002-2134, 33rd AIAA Plasmadynamics and Laser Conference, 20–23 May 2002, Maui, HI.
[42]S. B. Pope, *Turbulent Flows* (Cambridge University Press, Cambridge, 2000).
[43]D. V. Gaitonde, ''High-order solution procedure for three-dimensional non-ideal magnetogasdynamics,'' AIAA J. **39**, 2111 (2001).
[44]F. Ladeinde, E. E. O'Brien, and X. D. Cai, ''A parallelized ENO procedure for direct numerical simulation of compressible turbulence,'' J. Sci. Comput. **11**, 179 (1996).
[45]R. Ghosh and W. H. Matthaeus, ''Low Mach number two-dimensional hydrodynamic turbulence: Energy budget and density fluctuations in a polytropic fluid,'' Phys. Fluids A **4**, 148 (1992).
[46]H. Tennekes and J. L. Lumley, *A First Course in Turbulence* (MIT Press, Cambridge, MA, 1972).